

Electrically tunable dipolar interactions between layer-hybridized excitons

Daniel Erckensten,¹ Samuel Brem,² Raúl Perea-Causín,¹ Joakim Hagel,¹
Fedele Tagarelli,³ Edoardo Lopriore,³ Andras Kis,³ and Ermin Malic^{2,1}

¹*Department of Physics, Chalmers University of Technology, 41296 Gothenburg, Sweden*

²*Department of Physics, Philipps-Universität Marburg, 35037 Marburg, Germany*

³*Institute of Electrical and Microengineering, École Polytechnique Fédérale de Lausanne (EPFL), Lausanne, Switzerland*

Transition-metal dichalcogenide bilayers exhibit a rich exciton landscape including layer-hybridized excitons, i.e. excitons which are of partly intra- and interlayer nature. In this work, we study hybrid exciton-exciton interactions in naturally stacked WSe₂ homobilayers. In these materials, the exciton landscape is electrically tunable such that the low-energy states can be rendered more or less interlayer-like depending on the strength of the external electric field. Based on a microscopic and material-specific many-particle theory, we reveal two intriguing interaction regimes: a low-dipole regime at small electric fields and a high-dipole regime at larger fields, involving interactions between hybrid excitons with a substantially different intra- and interlayer composition in the two regimes. While the low-dipole regime is characterized by weak inter-excitonic interactions between intralayer-like excitons, the high-dipole regime involves mostly interlayer-like excitons which display a strong dipole-dipole repulsion and give rise to large spectral blue-shifts and a highly anomalous diffusion. Overall, our microscopic study sheds light on the remarkable electrical tunability of hybrid exciton-exciton interactions in atomically thin semiconductors and can guide future experimental studies in this growing field of research.

Recently, two-dimensional van der Waals heterostructures, formed by stacking transition-metal dichalcogenide monolayers on top of each other, have emerged as a promising platform for engineering strong correlations, topology and intriguing many-body interactions [1–5]. In particular, these structures exhibit spatially separated interlayer excitons, i.e., Coulomb-bound electron-hole pairs where the constituent electrons and holes reside in different layers, which display permanent out-of-plane dipole moments [6–10]. Furthermore, intra- and interlayer exciton states can be efficiently hybridized via electron and hole tunneling, and form new hybrid excitons (hX) that inherit properties of both exciton species [11–14]. The formation of hybrid excitons is particularly favorable in naturally stacked homobilayers, as opposed to type-II heterostructures where the dominating exciton species have mostly interlayer character [15, 16].

Moreover, the ground state of hybrid excitons can be optically inactive or momentum-dark [17], as is the case in WSe₂ homobilayers (Fig. 1(a)) [18, 19]. Here, the efficient electron tunneling at the Λ -point of the Brillouin zone (and less efficient hole tunneling at the K-point) results in a strongly hybridized KA exciton state [13]. Furthermore, in naturally stacked H-type (2H) WSe₂ homobilayers, the KA state is energetically degenerate with the $K'A'$ state, however these two states exhibit opposite dipole orientations (as a consequence of the inverted spin-orbit splitting in one of the layers [13]). This stacking configuration also enables the formation of other exciton species, such as KA' excitons, which lie energetically close to the degenerate KA and $K'A'$ states. Intriguingly, the KA' exciton state exhibits a much larger interlayer component than the KA state as schematically illustrated in Fig. 1(a) (where green and gray bands refer to the upper and lower TMD layer, respectively). As hybrid excitons are partly of interlayer character, they also exhibit an

out-of-plane dipole moment which couples to externally applied electric fields via the quantum-confined Stark effect [20–24], such that the interlayer component of these excitons and even the ordering of different hybrid exciton states can be tuned [25, 26]. This implies that also the interactions, in particular the dipole-dipole repulsion, between different types of hybrid excitons should be electrically tunable. Hence, a remarkable number of fundamentally and technologically relevant phenomena governed by exciton-exciton interactions in TMDs could potentially be electrically controlled. Some of these phenomena include experimentally observed blue-shifts of exciton resonances with excitation power [6, 27], anomalous exciton transport [28, 29], and even the stability of Bose-Einstein condensates [30, 31], the conditions for superfluidity [32–34] and the exciton compressibility that is important for the characterization of excitonic insulators [35].

In this work, we develop a material-specific and predictive many-particle theory of hybrid exciton-exciton interactions using the density matrix formalism. We investigate the impact of electric fields on density-dependent energy renormalizations and exciton transport at elevated excitation densities in naturally stacked WSe₂ homobilayers. We show that two intriguing interaction regimes emerge when applying an out-of-plane electric field: **(i)** a low-dipole regime at $E_z \lesssim 0.15$ V/nm (Fig. 1(b)), where interactions are governed by mostly intralayer-like KA and $K'A'$ excitons which mutually attract each other, and **(ii)** a high-dipole regime at $E_z \gtrsim 0.15$ V/nm (Fig. 1(c)), where mostly interlayer-like KA' excitons constitute the energetically lowest state which exhibits a strong dipole-dipole repulsion. These regimes give rise to substantially different behaviors for the experimentally accessible energy renormalizations and exciton transport. While the low-dipole regime is characterized by negligible exciton

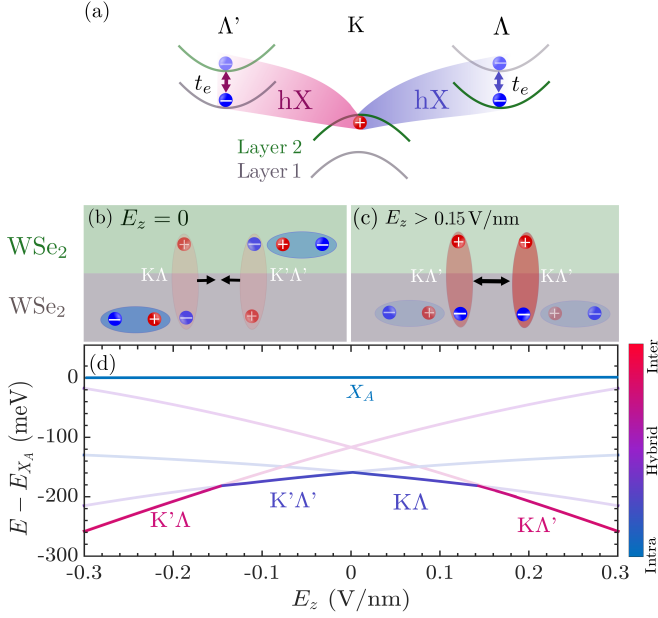


FIG. 1. Hybrid exciton species in naturally stacked bilayer WSe₂. **(a)**: KA and KA' hybrid excitons (hX) are primarily formed from electrons and holes in the same or different layers, respectively. The two layers are indicated with green and gray lines. The hybridization is predominantly induced via electron (t_e) tunneling. Note that the K'A' and K'A excitons, which are degenerate with the respective KA and KA' states and exhibit opposite dipole moments, are not shown. **(b)**: At vanishing electric fields the degenerate KA and K'A' hX are the energetically lowest states. These are mostly intralayer-like in nature and attract each other due to their opposite dipole moments. **(c)**: At electric fields $E_z > 0.15$ V/nm, KA' excitons constitute the energetically lowest states. These are mostly interlayer in nature and repel each other. **(d)**: Exciton landscape as a function of electric field, with the colorbar revealing a transition from a mostly intralayer-like (blue) to a mostly interlayer-like exciton state (red) at elevated electric fields. The thick line denotes the energetically lowest state that changes depending on the electric field. The energies are given with respect to the KK intralayer exciton (usually denoted as X_A in literature).

line-shifts and a conventional diffusion, the high-dipole regime exhibits considerable blue-shifts of tens of meVs and a highly anomalous diffusion. Overall, our work provides a recipe for future experiments on how to tune the hybrid exciton-exciton interaction and in particular exciton transport at elevated excitation powers.

HYBRID EXCITON LANDSCAPE

To model exciton-exciton interactions between layer-hybridized excitons in TMD bilayers, we first set up an excitonic Hamiltonian operator $H = H_{x,0} + H_{x-x}$ expressed in a monolayer eigenbasis [36]. Here, the first part of the Hamiltonian takes into account the centre-of-mass motion of intra- and interlayer excitons, their Coulomb

binding, and their hybridization via an effective tunneling model. The Hamiltonian which captures exciton hybridization reads [13, 37]

$$H_{x,0} = \sum_{\xi, L, L', \mathbf{Q}} (E_{L, \mathbf{Q}}^{\xi} \delta_{L, L'} + T_{LL'}^{\xi}) X_{L, \mathbf{Q}}^{\dagger \xi} X_{L', \mathbf{Q}}^{\xi}, \quad (1)$$

with the first term being the exciton dispersion $E_{L, \mathbf{Q}}^{\xi} = \frac{\hbar^2 \mathbf{Q}^2}{2M^{\xi L}} + E_b^{\xi L} + \Delta^{\xi L}$, and the exciton binding energy, $E_b^{\xi L}$, obtained from solving the bilayer Wannier equation [19, 38]. Here, $M^{\xi L}$ is the total exciton mass, $L = (l_h, l_e)$ is a compound layer index, $\xi = (\xi_h, \xi_e)$ is the exciton valley and \mathbf{Q} is the centre-of-mass momentum. Furthermore, $\Delta^{\xi L}$ contains the valley-specific band gap. Note that, due to the degeneracy between exciton states with different spin-valley configurations (neglecting electron-hole exchange [39]), it is sufficient to consider a single spin system, e.g. exciton states being formed by spin-up valence and conduction bands, so that spin indices can be omitted. The excitonic operators $X_{L, \mathbf{Q}}^{\dagger \xi}$ ($X_{L, \mathbf{Q}}^{\xi}$) create (annihilate) intralayer (X , $l_e = l_h$) or interlayer (IX , $l_e \neq l_h$) excitons. The second part of Eq. (1) takes into account the tunneling of electrons and holes between different layers via the excitonic tunneling matrix element, $T_{LL'}^{\xi}$ [19]. The latter is dependent on electron/hole tunneling strengths and excitonic wave function overlaps, cf. Supplementary Section I for details. By performing the basis transformation $X_{L, \mathbf{Q}}^{\dagger \xi} = \sum_{\eta} Y_{\eta, \mathbf{Q}}^{\dagger \xi} C_{L, \mathbf{Q}}^{\xi \eta}$, introducing the *hybrid* exciton operators Y_{η}^{\dagger} , the hybrid exciton state η , and the mixing coefficients C determining the relative intra- and interlayer content of the hybrid exciton, the Hamiltonian in Eq. (1) is diagonalized and becomes

$$\tilde{H}_{x,0} = \sum_{\xi, \eta, \mathbf{Q}} E_{\eta, \mathbf{Q}}^{(hX)\xi} Y_{\eta, \mathbf{Q}}^{\dagger \xi} Y_{\eta, \mathbf{Q}}^{\xi}, \quad (2)$$

where the hybrid exciton dispersion $E_{\eta, \mathbf{Q}}^{(hX)\xi}$ along with the mixing coefficients are obtained from solving the hybrid exciton eigenvalue problem, cf. Supplementary Section I. In this work, we are only concerned with the lowest hybrid exciton state η , and omit this index in the following. In Fig. 1(d), we show the hybrid exciton landscape for an hBN-encapsulated and naturally stacked (2H) WSe₂ homobilayer, including the four lowest-lying states. In Table S1 in Supplementary Section I, we include also higher-lying transitions. The hybrid exciton eigenenergy $E \equiv E_{\mathbf{Q}=0}^{(hX)}$ is given relative to the intralayer A exciton energy, E_{X_A} . We find that $\xi = (\xi_h, \xi_e) = \text{KA/K'A'}$ exciton states constitute the energetically lowest states, lying approximately 160 meV below the bright X_A state. The colorbar indicates the corresponding interlayer component of the mixing coefficient, revealing the hybrid nature of KA/K'A' excitons, cf. Fig. 1(d) at $E_z = 0$.

Furthermore, we study the exciton landscape as a function of an out-of-plane electric field, E_z . This is done

by exploiting the electrostatic Stark shifts of the interlayer exciton energies, which influence the intra- and interlayer composition of hybrid excitons [20, 22, 24]. Intriguingly, we find that for positive (negative) electric fields $|E_z| > 0.15$ V/nm, the energetically lowest state corresponds to the KA' ($\text{K}'\text{A}$) state, i.e. the ordering of different exciton states is changed. This is explained by the fact that, as a consequence of the band-ordering (Fig. 1(a)), the KA' state carries a significantly larger interlayer component than the KA state and is as such easier modulated with respect to electric fields. In particular, the KA' and KA states possess an interlayer component $|C_{IX}|^2$ of 0.64 (0.80) and 0.23 (0.39), respectively, at $E_z = 0$ (0.3) V/nm. The fact that the dominating exciton species at elevated electric fields carries a large interlayer component and consequently a large dipole moment is also reflected in the stronger exciton-exciton interaction, as we shall see in the following.

HYBRID EXCITON-EXCITON INTERACTIONS

Now, we consider the interacting part of the Hamiltonian, H_{x-x} . In this work, we focus on the direct part of the interaction, and the contributions from interlayer excitons. Interlayer exchange interactions are seen to give a minor correction to the direct dipole-dipole interaction [42, 43]. Although intralayer exchange interactions (taking into account exchange of individual carriers) are dominant in TMD monolayers [44, 45], they are known to have a negligible impact on experimentally accessible density-dependent energy renormalizations, as their contributions are largely cancelled out against contributions due to higher-order correlation effects [46, 47]. This is also supported by recent experiments, which report negligible shifts with excitation power of intralayer exciton resonances and sizable blue-shifts in luminescence spectra for interlayer excitons [6, 28]. Furthermore, we assumed that the excitons can be treated as independent bosons, which holds in the weakly interacting limit $n_x a_B^2 \ll 1$, where a_B is the exciton Bohr radius and n_x is the exciton density [48].

We transform the interaction Hamiltonian to the hybrid basis (cf. Supplementary Section II for details) resulting in

$$\tilde{H}_{x-x} = \frac{1}{2A} \sum_{\xi, \xi', q, Q, Q'} \tilde{W}_q^{\xi\xi'} Y_{Q+q}^{\dagger\xi} Y_{Q'-q}^{\dagger\xi'} Y_{Q'}^\xi Y_Q^\xi, \quad (3)$$

with the hybrid dipole-dipole interaction matrix element $\tilde{W}_q^{\xi\xi'} = \sum_{i,j=1,2} W_{IX_i, IX_j, q}^{\xi\xi'} |C_{IX_i}^\xi|^2 |C_{IX_j}^{\xi'}|^2$ and the normalization area A . The hybrid exciton-exciton interaction crucially includes the pure interlayer dipole-dipole interaction between different interlayer exciton species IX_i , $i = 1, 2$, weighted by the corresponding mixing coefficients. The interlayer dipole-dipole matrix element reads in the long wavelength limit $W_{IX_i, IX_i, q \rightarrow 0}^{\xi\xi'} = -W_{IX_i, IX_j, q \rightarrow 0}^{\xi\xi'}$ where $i \neq j$ and with $d_{\text{TMD}} = \frac{d_{\text{TMD}} \epsilon_0^2}{2\epsilon_0 \epsilon_{\text{TMD}}}$,

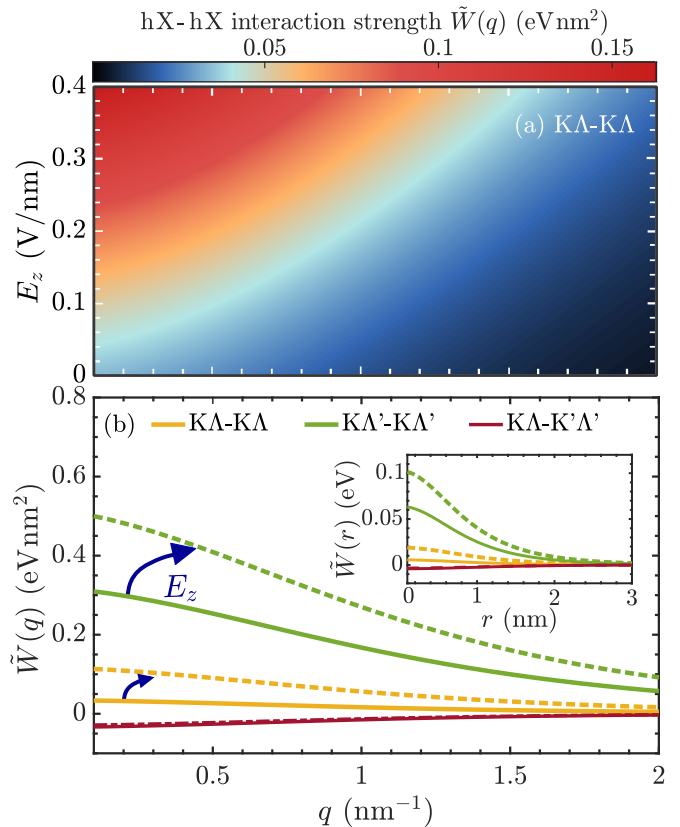


FIG. 2. Hybrid exciton-exciton interactions. **(a)**: Momentum- and electric-field dependent interaction strength involving KA hX. The interaction strength increases as the interlayer component is enhanced under the application of an out-of-plane electric field, E_z . **(b)**: Momentum-dependent interaction strengths for different electric fields and between different types of hybrid excitons. Solid lines correspond to the case $E_z = 0$ and dashed lines to the case of $E_z = 0.3$ V/nm. The inset shows the corresponding real-space interaction, $\tilde{W}(r)$.

and $\epsilon_{\text{TMD}}^\perp$ being the TMD thickness and the out-of-plane component of the dielectric tensor of the TMD, respectively. The sign difference between the interactions is a consequence of the opposite dipole orientations of the interlayer excitons IX_1 and IX_2 (cf. Fig. 1(b)). The full hybrid Hamiltonian including intra- and interlayer direct and exchange contributions is derived in Supplementary Section II.

In Fig. 2(a), we display the hybrid exciton-exciton interaction matrix element for $\xi = \xi' = \text{KA}$ hybrid excitons as a function of momentum and out-of-plane electric field. The interaction is repulsive (> 0) and maximized in the long wavelength limit. The interaction strength is also found to be highly tunable with respect to electric fields via its quartic dependence on interlayer mixing coefficients (cf. Eq. (3)). In particular, the interlayer component of hybrid excitons is enhanced with E_z , if the electric field is applied parallel to the dipole moment of the hX, cf. Fig. 1(c). In Fig. 2(b), we consider inter-

actions between different types of hybrid exciton species at vanishing electric fields (solid lines) and at $E_z = 0.3$ V/nm (dashed lines). Due to their large interlayer component (Fig. 1(d)), KA' excitons exhibit the strongest dipole-dipole repulsion, which is further enhanced with E_z . Furthermore, we note that the interaction between KA and $\text{K}'\Lambda'$ excitons is attractive (<0), cf. Fig. 1(b). This is a consequence of the interlayer component of these excitons having opposite dipole moments. As such, the exciton states energetically shift in opposite directions under the application of an electric field and the increase of interlayer component in one of the excitons is compensated by a decrease of interlayer component in the other exciton (Fig. 1(d)). This yields an interaction strength which is largely independent on electric field. We also show the hybrid exciton-exciton interaction in real space (inset in Fig. 2(b)), and identify the dipole-dipole-like character of the interaction between excitons of the same valley species at large distances, i.e. $\tilde{W}(r) \sim d_{\text{TMD}}^2/r^3$ (cf. Supplementary Section III) [49, 50]. Finally, we note that the real-space exciton-exciton interaction, crucially including the dipole-dipole interaction, is a key ingredient in the Bose-Hubbard model, which can be exploited to investigate the conditions for different quantum phases of excitonic systems, such as superfluidity, in semiconductor moiré materials [32, 33, 51].

Having microscopic access to the hybrid exciton-exciton interaction matrix elements enables us to study density-dependent energy renormalizations observable in photoluminescence (PL) spectra. In particular, given the large electrical tunability of exciton-exciton interactions, we expect that applying electric fields in combination with increasing pump power can be used to engineer substantial blue-shifts of exciton luminescence peaks. This offers an intriguing way of realizing strong many-body interactions in atomically thin semiconductors. Note that the relevant excitons in homobilayer WSe_2 are momentum-dark (Fig. 1(a)), and become only visible via phonon sidebands in low-temperature PL [22, 26, 52–54]. In our theoretical model, we derive the density-dependent energy renormalization δE^ξ by evaluating the Heisenberg equation of motion for the hybrid polarization on a Hartree-Fock (mean-field) level and find

$$\delta E^\xi = \sum_{\xi_1} \left(\tilde{W}_0^{\xi\xi_1\xi_1\xi} + \tilde{W}_0^{\xi\xi_1\xi\xi_1} \right) n_{x_1}^{\xi_1} = \frac{d^\xi e_0^2}{\epsilon_0 \epsilon_{\text{TMD}}^\perp} n_x, \quad (4)$$

where the first term reflects direct exciton-exciton interactions and the second term is due to exciton exchange [55], with the interaction matrix element $\tilde{W}_q^{\xi_1\xi_2\xi_3\xi_4} \equiv \delta_{\xi_1,\xi_4} \delta_{\xi_2,\xi_3} \tilde{W}_q^{\xi_1\xi_2}$ (cf. Eq. (3)). The interaction matrix elements are evaluated in the long wavelength limit, such that the energy renormalization becomes momentum-independent. This is well justified when the exciton distribution is strongly peaked around small centre-of-momenta, i.e. at lower temperatures. The interaction strength is weighted by the valley-specific hybrid exciton density $n_x^\xi = \frac{1}{A} \sum_{\xi, \mathbf{Q}} N_{\mathbf{Q}}^{(hX)\xi}$, and the exciton occu-

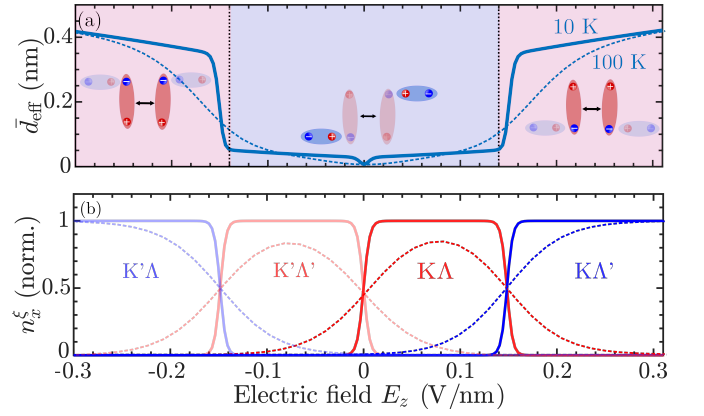


FIG. 3. Dipole length of hybrid excitons. **(a)**: Average dipole length \bar{d}_{eff} as a function of electric field revealing a drastic increase of the dipole length for $|E_z| > 0.15$ V/nm at low temperatures ($T = 10$ K). This is explained by a large valley-specific dipole length d_{eff}^ξ of mostly interlayer-like $\xi = \text{KA}'/\text{K}'\Lambda$ excitons and a predominant occupation n_x^ξ of these excitons at elevated electric fields shown in **(b)**. The average dipole length and valley occupations at $T = 100$ K are shown as dashed lines.

pation is estimated by a thermalized Boltzmann distribution $N_{\mathbf{Q}}^{(hX)\xi} \sim n_x \exp(-E_{\mathbf{Q}}^{(hX)\xi}/(k_B T))$ such that the energy renormalization scales linearly with the total exciton density $n_x = \sum_{\xi} n_x^\xi$. This allows us to absorb the exciton-exciton interaction strength and relative occupations in an effective valley-dependent dipole length d^ξ . In this way, the energy renormalization of a single exciton species ξ is completely characterized by its effective dipole length. A detailed derivation of Eq. (4) and the relevant (electric field-dependent) valley-specific dipole lengths are found in Supplementary Section IV.

Furthermore, we define an *average* effective dipole length of the exciton gas, $\bar{d}_{\text{eff}} = n_x^{-1} \sum_{\xi} d^\xi n_x^\xi$. This quantity is crucial to access macroscopic transport properties, as further discussed in the next section. The average effective dipole length is presented in Fig. 3(a) as function of electric field, together with the normalized valley-specific exciton density in Fig. 3(b). At low electric fields, the exciton occupation is shared between the energetically degenerate KA and $\text{K}'\Lambda'$ states (cf. also Fig. 1(d)). These excitons interact weakly via dipolar interactions and combined with their attractive mutual interaction this results in suppressed average effective dipole lengths, $\bar{d}_{\text{eff}} \approx 0.01$ nm. In contrast, at elevated electric fields $|E_z| > 0.15$ V/nm, $\text{KA}'/\text{K}'\Lambda$ excitons are found to give rise to large effective dipole lengths $\bar{d}_{\text{eff}} \approx 0.4$ nm, reflecting their large occupation (Fig. 3(b)) as well as their large interaction strength (Fig. 2(b)). Here, we remark that the extracted effective dipole length at large electric fields can be compared with the dipole length of a pure interlayer exciton, d_{IX} , here assumed to be equal to the TMD layer thickness, $d_{\text{TMD}} = 0.65$ nm (Supplementary Section I). In particular, it holds that

ANOMALOUS HYBRID EXCITON TRANSPORT

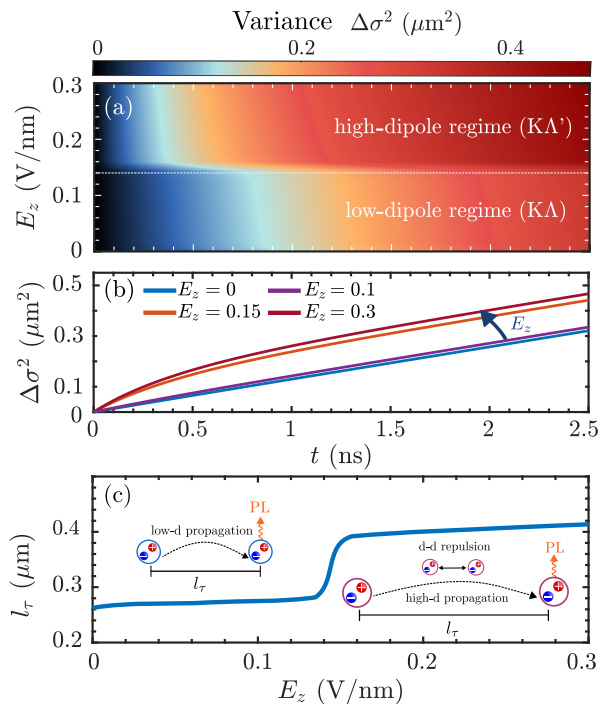


FIG. 4. Tunability of hybrid exciton diffusion. **(a)**: Electric-field dependent and time-dependent variances $\Delta\sigma^2 = \sigma_t^2 - \sigma_0^2$ for the exciton density $n(\mathbf{r}, t)$, revealing highly anomalous diffusion for electric fields $E_z > 0.15$ V/nm at $T = 10$ K. The dashed white line indicates the transition from the low-dipole regime (dominated by $K\Lambda$ excitons) to the high-dipole regime (dominated by $K\Lambda'$ excitons). **(b)**: Time-dependent variances for different electric fields. For low electric fields ($E_z \leq 0.15$ V/nm) conventional diffusion is observed, while at higher electric fields the variance varies non-linearly with time—a hallmark of anomalous diffusion. **(c)**: Diffusion length l_τ as a function of electric field. At large electric fields strong dipole-dipole repulsion between $K\Lambda'$ excitons is present, resulting in significantly increased diffusion lengths.

$\bar{d}_{\text{eff}} = d_{IX}|C_{IX}^{K\Lambda'}|^4 \approx 0.4$ nm, i.e. the effective dipole length is obtained by weighting the pure interlayer exciton dipole length by the interlayer component of the mixing coefficient. Furthermore, we note that the transition between the low-dipole regime in which $K\Lambda$ and $K'\Lambda'$ excitons are prevalent and the high-dipole regime dominated by $K\Lambda'$ or $K'\Lambda$ excitons can be tuned by raising the temperature, cf. the dashed curve in Fig. 3(a) displaying the average effective dipole length at $T = 100$ K. This is a consequence of intralayer-like and interlayer-like exciton states being simultaneously populated at high temperatures. Considering the case of $T = 100$ K, there exists a sizable occupation of $K\Lambda/K'\Lambda'$ excitons at finite electric fields and a large electric field ($|E_z| \approx 0.3$ V/nm) is therefore required for the high-dipole ($K\Lambda'/K'\Lambda$) regime to be reached (cf. dashed lines in Fig. 3(b)).

For a spatially dependent exciton density $n_x \rightarrow n(\mathbf{r})$, the density-dependent energy renormalization due to repulsive exciton-exciton interactions gives rise to a drift force $-\nabla(\delta E(\mathbf{r}))$. The latter drags excitons away from the excitation spot [28, 29, 56] in analogy to exciton funneling in strain potentials [57]. This can be described by the two-dimensional drift-diffusion equation for the exciton density:

$$\partial_t n(\mathbf{r}, t) = D\nabla^2 n + \mu\nabla \cdot (\nabla(\delta\bar{E})n) - \frac{n}{\tau}, \quad (5)$$

which is derived using the Wigner function formalism [43, 58]. Here, D is the diffusion coefficient governing the free propagation of excitons, $\mu = \frac{D}{k_B T}$ is the exciton mobility, T being temperature and τ is the exciton life-time. The second term in Eq. (5) is the drift-term dictated by the averaged energy renormalization $\delta\bar{E}(n(\mathbf{r}, t)) \equiv \frac{d_{\text{eff}}^2 e_0^2}{\epsilon_0 \epsilon_{\text{TMD}}} n(\mathbf{r}, t)$, in which the average effective dipole length d_{eff} crucially enters (Fig. 3(a)). In order to arrive at Eq. (5), we assumed that all exciton states ξ which contribute to the total exciton population $n = \sum_{\xi} n^{\xi}$ diffuse with the same diffusion coefficient $D^{\xi} \approx D$ and that the total population is in thermal equilibrium with the lattice. The first assumption is reasonable since the diffusion coefficient is mainly determined by the effective exciton mass, which is the same in the considered states. The slow thermal equilibration of the exciton gas at low temperatures can, in principle, influence the diffusion dynamics [59], but these effects have not been observed for the exciton diffusion in van der Waals heterostructures even at cryogenic temperatures [29].

We now make use of the strong tunability of the dipole length to show that also the exciton transport can be tuned with respect to electric fields. By numerically solving Eq. (5) we obtain a microscopic access to the spatiotemporal dynamics of excitons. We initialize the exciton density as a typical Gaussian-shaped laser pulse, i.e. $n(x, y, 0) = n_0 \exp(-(x^2 + y^2)/\sigma_0^2)$ with the initial spot size $\sigma_0^2 = 1 \mu\text{m}^2$ and set the temperature $T = 10$ K. The initial exciton density is set to $n_0 = 10^{12} \text{ cm}^{-2}$, such that the drift due to exciton-exciton interactions becomes important and Boltzmann distributions can be used to model the spatiotemporal dynamics of excitons [43]. The considered initial exciton density is below the exciton Mott transition, which is estimated to occur at densities $\sim 7 \cdot 10^{12} \text{ cm}^{-2}$ in WSe_2 homobilayers [60] and we neglect the impact of free carriers on the transport [61]. Moreover, we assume the diffusion coefficient $D = 0.3 \text{ cm}^2/\text{s}$ and the exciton life-time $\tau = 500$ ps as obtained from a recent experiment on the same homobilayer [62]. Note that there is no moiré potential which could trap excitons and slow down their propagation [28, 63–65], as we are considering untwisted homobilayers with no lattice mismatch.

In Fig. 4(a), the time- and electric-field dependent variance $\Delta\sigma^2 = \sigma_t^2 - \sigma_0^2$ is shown for the case of naturally stacked hBN-encapsulated WSe₂ homobilayers, revealing a significant broadening of the exciton spatial distribution at electric fields $E_z > 0.15$ V/nm, corresponding to the high-dipole regime (cf. Fig. 3(a)). The transition from the low-dipole to the high-dipole regime results in highly non-linear exciton transport, cf. Fig. 4(b). In the low-dipole regime (Fig. 3(a)), excitons are not affected by any drift and the width of the distribution varies approximately linearly with time, i.e. $\Delta\sigma^2 = 4Dt$ according to Fick's law. In contrast, in the high-dipole regime, the exciton drift is highly efficient leading to a super-linear dependence on the variance with respect to time—a hallmark of anomalous diffusion [28]. Finally, given the fully time-resolved broadening of the exciton distribution, we extract a time-independent measure of the exciton transport, i.e. the experimentally tractable diffusion length $l_\tau = 2\sqrt{D_\tau\tau} = \sqrt{\sigma_\tau^2 - \sigma_0^2}$ [66]. This quantity is a measure for how far away from the excitation spot the excitons propagate before recombining and should thus be enhanced with the exciton drift due to dipole-dipole repulsion (Fig. 4(c)). We obtain diffusion lengths in the submicrometer range, concretely 0.25 μm and 0.40 μm in the low- and high-dipole regime, respectively, which are similar to diffusion lengths obtained from previous transport measurements on TMD monolayers and bilayers [63, 67]. We note that excitons in MoSe₂/hBN/WSe₂ heterostructures have been reported to exhibit longer diffusion lengths of 1 – 2 μm [29], since excitons in these structures are of purely interlayer character and exhibit enhanced dipole moments due to the hBN spacer. Overall, we reveal a remarkable tunability of the diffusion length in the considered WSe₂ bilayers with electric fields and we find that the transport of hybrid excitons can be electrically controlled, which is of importance for the realization of exciton-based optoelectronic devices [68, 69].

CONCLUSIONS

Our work sheds light on the impact of electric fields on hybrid exciton-exciton interactions in transition-metal dichalcogenide bilayers. We highlight the presence of hybrid excitons in naturally-stacked WSe₂ homobilayers and find that the energetically lowest exciton state in these structures can be tuned by applying an out-of-plane electric field. The nature of the lowest state varies from mostly intralayer to mostly interlayer character, resulting in a low-dipole and a high-dipole regime at small and large electric fields, respectively. The latter is characterized by strong interactions between hybrid excitons due to the efficient dipole-dipole repulsion. The electrical tunability of the interactions has also direct consequences on exciton transport. In particular, we predict that the transition from low- to high-dipole regime is accompanied by the emergence of anomalous exciton diffusion, which is a characteristic fingerprint of strong dipole-dipole repulsion. The insights obtained from our material-specific and predictive many-particle theory can be used to guide experiments to measure the tunability of hybrid exciton-exciton interactions in atomically thin semiconductors. Furthermore, our study provides tools for investigating the impact of electrically tunable exciton-exciton interactions on other exotic phenomena in semiconductor moiré materials such as exciton condensation and superfluidity.

ACKNOWLEDGMENTS

We thank Roberto Rosati (Philipps-Universität Marburg) for useful discussions. This project has received funding from Deutsche Forschungsgemeinschaft via CRC 1083 and the project 512604469 as well as from the European Unions Horizon 2020 research and innovation programme under grant agreement no. 881603 (Graphene Flagship). The Kis group received funding from the Swiss National Science Foundation (grants no. 164015, 177007, 175822, 205114), and the Marie Curie Skłodowska ITN network “2-Exciting” (grant no. 956813).

-
- [1] A. K. Geim and I. V. Grigorieva, *Nature* **499**, 419 (2013).
 - [2] K. F. Mak and J. Shan, *Nature Nanotechnology* **17**, 686 (2022).
 - [3] Y. Xu, K. Kang, K. Watanabe, T. Taniguchi, K. F. Mak, and J. Shan, *Nature Nanotechnology* **17**, 934 (2022).
 - [4] T. Mueller and E. Malic, *npj 2D Materials and Applications* **2**, 1 (2018).
 - [5] R. Perea-Causin, D. Erckensten, J. M. Fitzgerald, J. J. P. Thompson, R. Rosati, S. Brem, and E. Malic, *APL Materials* **10**, 100701 (2022).
 - [6] P. Nagler, G. Plechinger, M. V. Ballottin, A. Mitioglu, S. Meier, N. Paradiso, C. Strunk, A. Chernikov, P. C. Christianen, C. Schüller, *et al.*, *2D Materials* **4**, 025112 (2017).
 - [7] P. Merkl, F. Mooshammer, P. Steinleitner, A. Girnguber, K.-Q. Lin, P. Nagler, J. Holler, C. Schüller, J. M. Lupton, T. Korn, *et al.*, *Nature Materials* **18**, 691 (2019).
 - [8] D. Schmitt, J. P. Bange, W. Bennecke, A. AlMutairi, G. Meneghini, K. Watanabe, T. Taniguchi, D. Steil, D. R. Luke, R. T. Weitz, *et al.*, *Nature* **608**, 499 (2022).
 - [9] B. Miller, A. Steinhoff, B. Pano, J. Klein, F. Jahnke, A. Holleitner, and U. Wurstbauer, *Nano Letters* **17**, 5229 (2017).

- [10] A. Ciarrocchi, F. Tagarelli, A. Avsar, and A. Kis, *Nature Reviews Materials* **7**, 449 (2022).
- [11] E. M. Alexeev, D. A. Ruiz-Tijerina, M. Danovich, M. J. Hamer, D. J. Terry, P. K. Nayak, S. Ahn, S. Pak, J. Lee, J. I. Sohn, *et al.*, *Nature* **567**, 81 (2019).
- [12] D. A. Ruiz-Tijerina and V. I. Fal'ko, *Physical Review B* **99**, 125424 (2019).
- [13] S. Brem, K.-Q. Lin, R. Gillen, J. M. Bauer, J. Maultzsch, J. M. Lupton, and E. Malic, *Nanoscale* **12**, 11088 (2020).
- [14] N. Peimyo, T. Deilmann, F. Withers, J. Escolar, D. Nutting, T. Taniguchi, K. Watanabe, A. Taghizadeh, M. F. Craciun, K. S. Thygesen, *et al.*, *Nature Nanotechnology* **16**, 888 (2021).
- [15] R. Gillen and J. Maultzsch, *Physical Review B* **97**, 165306 (2018).
- [16] S. Latini, K. T. Winther, T. Olsen, and K. S. Thygesen, *Nano Science* **17**, 938 (2017).
- [17] J. Kunstmann, F. Mooshammer, P. Nagler, A. Chaves, F. Stein, N. Paradiso, G. Plechinger, C. Strunk, C. Schüller, G. Seifert, *et al.*, *Nature Physics* **14**, 801 (2018).
- [18] T. Deilmann and K. S. Thygesen, *2D Materials* **6**, 035003 (2019).
- [19] J. Hagel, S. Brem, C. Linderälv, P. Erhart, and E. Malic, *Physical Review Research* **3**, 043217 (2021).
- [20] N. Leisgang, S. Shree, I. Paradisanos, L. Sponfeldner, C. Robert, D. Lagarde, A. Balocchi, K. Watanabe, T. Taniguchi, X. Marie, *et al.*, *Nature Nanotechnology* **15**, 901 (2020).
- [21] L. A. Jauregui, A. Y. Joe, K. Pistunova, D. S. Wild, A. A. High, Y. Zhou, G. Scuri, K. De Greve, A. Sushko, C.-H. Yu, *et al.*, *Science* **366**, 870 (2019).
- [22] Z. Wang, Y.-H. Chiu, K. Honz, K. F. Mak, and J. Shan, *Nano Letters* **18**, 137 (2018).
- [23] E. Lopriore, E. G. Marin, and G. Fiori, *Nanoscale Horizons* **7**, 41 (2022).
- [24] T. Deilmann and K. S. Thygesen, *Nano letters* **18**, 2984 (2018).
- [25] J. Hagel, S. Brem, and E. Malic, *2D Materials* **10**, 014013 (2022).
- [26] Z. Huang, Y. Zhao, T. Bo, Y. Chu, J. Tian, L. Liu, Y. Yuan, F. Wu, J. Zhao, L. Xian, K. Watanabe, T. Taniguchi, R. Yang, D. Shi, L. Du, Z. Sun, S. Meng, W. Yang, and G. Zhang, *Physical Review B* **105**, L041409 (2022).
- [27] D. Unuchek, A. Ciarrocchi, A. Avsar, Z. Sun, K. Watanabe, T. Taniguchi, and A. Kis, *Nature nanotechnology* **14**, 1104 (2019).
- [28] L. Yuan, B. Zheng, J. Kunstmann, T. Brumme, A. B. Kuc, C. Ma, S. Deng, D. Blach, A. Pan, and L. Huang, *Nature Materials* **19**, 617 (2020).
- [29] Z. Sun, A. Ciarrocchi, F. Tagarelli, J. F. Gonzalez Marin, K. Watanabe, T. Taniguchi, and A. Kis, *Nature Photonics* **16**, 79 (2022).
- [30] Z. Wang, D. A. Rhodes, K. Watanabe, T. Taniguchi, J. C. Hone, J. Shan, and K. F. Mak, *Nature* **574**, 76 (2019).
- [31] Q. Shi, E.-M. Shih, D. Rhodes, B. Kim, K. Barmak, K. Watanabe, T. Taniguchi, Z. Papić, D. A. Abanin, J. Hone, *et al.*, *Nature Nanotechnology* , 1 (2022).
- [32] N. Götting, F. Lohof, and C. Gies, *Physical Review B* **105**, 165419 (2022).
- [33] C. Lagoin and F. Dubin, *Physical Review B* **103**, L041406 (2021).
- [34] M. Fogler, L. Butov, and K. Novoselov, *Nature Communications* **5**, 1 (2014).
- [35] L. Ma, P. X. Nguyen, Z. Wang, Y. Zeng, K. Watanabe, T. Taniguchi, A. H. MacDonald, K. F. Mak, and J. Shan, *Nature* **598**, 585 (2021).
- [36] F. Katsch, M. Selig, A. Carmele, and A. Knorr, *physica status solidi (b)* **255**, 1800185 (2018).
- [37] P. Merkl, F. Mooshammer, S. Brem, A. Girnghuber, K.-Q. Lin, L. Weigl, M. Liebich, C.-K. Yong, R. Gillen, J. Maultzsch, *et al.*, *Nature Communications* **11**, 1 (2020).
- [38] M. Kira and S. W. Koch, *Progress in quantum electronics* **30**, 155 (2006).
- [39] D. Y. Qiu, T. Cao, and S. G. Louie, *Phys. Rev. Lett.* **115**, 176801 (2015).
- [40] Z. Li, J. Förste, K. Watanabe, T. Taniguchi, B. Urbaszek, A. S. Baimuratov, I. C. Gerber, A. Högele, and I. Bilgin, *Phys. Rev. B* **106**, 045411 (2022).
- [41] J. Förste, N. V. Tepliakov, S. Y. Kruchinin, J. Lindlau, V. Funk, M. Förg, K. Watanabe, T. Taniguchi, A. S. Baimuratov, and A. Högele, *Nature Communications* **11**, 4539 (2020).
- [42] F.-C. Wu, F. Xue, and A. H. MacDonald, *Phys. Rev. B* **92**, 165121 (2015).
- [43] D. Erckensten, S. Brem, R. Perea-Causín, and E. Malic, *Physical Review Materials* **6**, 094006 (2022).
- [44] V. Shahnazaryan, I. Iorsh, I. A. Shelykh, and O. Kyriienko, *Physical Review B* **96**, 115409 (2017).
- [45] D. Erckensten, S. Brem, and E. Malic, *Physical Review B* **103**, 045426 (2021).
- [46] C. Trovatiello, F. Katsch, Q. Li, X. Zhu, A. Knorr, G. Cerullo, and S. Dal Conte, *Nano Letters* **22**, 5322 (2022).
- [47] F. Katsch, M. Selig, and A. Knorr, *2D Materials* **7**, 015021 (2019).
- [48] S. B.-T. De-Leon and B. Laikhtman, *Physical Review B* **63**, 125306 (2001).
- [49] R. Oldziejewski, A. Chiochetta, J. Knörzer, and R. Schmidt, *Physical Review B* **106**, L081412 (2022).
- [50] C. Schindler and R. Zimmermann, *Physical Review B* **78**, 045313 (2008).
- [51] C. Lagoin, U. Bhattacharya, T. Grass, R. Chhajlany, T. Salamon, K. Baldwin, L. Pfeiffer, M. Lewenstein, M. Holzmann, and F. Dubin, *Nature* **609**, 485 (2022).
- [52] J. Lindlau, M. Selig, A. Neumann, L. Colombier, J. Förste, V. Funk, M. Förg, J. Kim, G. Berghäuser, T. Taniguchi, *et al.*, *Nature communications* **9**, 1 (2018).
- [53] S. Brem, A. Ekman, D. Christiansen, F. Katsch, M. Selig, C. Robert, X. Marie, B. Urbaszek, A. Knorr, and E. Malic, *Nano Letters* **20**, 2849 (2020).
- [54] M. He, P. Rivera, D. Van Tuan, N. P. Wilson, M. Yang, T. Taniguchi, K. Watanabe, J. Yan, D. G. Mandrus, H. Yu, *et al.*, *Nature Communications* **11**, 1 (2020).
- [55] C. Ciuti, V. Savona, C. Piermarocchi, A. Quattropani, and P. Schwendimann, *Physical Review B* **58**, 7926 (1998).
- [56] A. Ivanov, *EPL (Europhysics Letters)* **59**, 586 (2002).
- [57] R. Rosati, R. Schmidt, S. Brem, R. Perea-Causín, I. Niehues, J. Kern, J. A. Preuß, R. Schneider, S. Michaelis de Vasconcellos, R. Bratschitsch, *et al.*, *Nature Communications* **12**, 1 (2021).
- [58] O. Hess and T. Kuhn, *Physical Review A* **54**, 3347 (1996).

- [59] R. Rosati, R. Perea-Causín, S. Brem, and E. Malic, *Nanoscale* **12**, 356 (2020).
- [60] T. Siday, F. Sandner, S. Brem, M. Zizlsperger, R. Perea-Causin, F. Schiegl, S. Nerreter, M. Plankl, P. Merkl, F. Mooshammer, *et al.*, *Nano Letters* **22**, 2561 (2022).
- [61] F. Lengers, R. Rosati, T. Kuhn, and D. E. Reiter, *Phys. Rev. B* **99**, 155306 (2019).
- [62] F. Tagarelli, E. Lopriore, D. Erkensten, R. Perea-Causin, S. Brem, J. Hagel, Z. Sun, G. Pasquale, K. Watanabe, T. Taniguchi, E. Malic, and A. Kis, *Nature Photonics*, 1–7 (2023).
- [63] J. Choi, W.-T. Hsu, L.-S. Lu, L. Sun, H.-Y. Cheng, M.-H. Lee, J. Quan, K. Tran, C.-Y. Wang, M. Staab, *et al.*, *Science Advances* **6**, eaba8866 (2020).
- [64] J. Wang, Q. Shi, E.-M. Shih, L. Zhou, W. Wu, Y. Bai, D. Rhodes, K. Barmak, J. Hone, C. R. Dean, and X.-Y. Zhu, *Physical Review Letters* **126**, 106804 (2021).
- [65] W. Knorr, S. Brem, G. Meneghini, and E. Malic, *Physical Review Materials* **6**, 124002 (2022).
- [66] M. Kulig, J. Zipfel, P. Nagler, S. Blanter, C. Schüller, T. Korn, N. Paradiso, M. M. Glazov, and A. Chernikov, *Physical Review Letters* **120**, 207401 (2018).
- [67] F. Cadiz, C. Robert, E. Courtade, M. Manca, L. Martinelli, T. Taniguchi, K. Watanabe, T. Amand, A. Rowe, D. Paget, *et al.*, *Applied Physics Letters* **112**, 152106 (2018).
- [68] D. Unuchek, A. Ciarrocchi, A. Avsar, K. Watanabe, T. Taniguchi, and A. Kis, *Nature* **560**, 340 (2018).
- [69] A. Ciarrocchi, D. Unuchek, A. Avsar, K. Watanabe, T. Taniguchi, and A. Kis, *Nature Photonics* **13**, 131 (2019).

Supplementary Material for Electrically tunable dipolar interactions between layer-hybridized excitons

Daniel Erckensten¹, Samuel Brem², Raúl Perea-Causín¹, Joakim Hagel¹,
Fedele Tagarelli³, Edoardo Lopriore³, Andras Kis³ and Ermin Malic^{2,1}

¹Department of Physics, Chalmers University of Technology, 41296 Gothenburg, Sweden

²Department of Physics, Philipps-Universität Marburg, 35037 Marburg, Germany

³Institute of Electrical and Microengineering, École Polytechnique Fédérale de Lausanne (EPFL), Lausanne, Switzerland

I. HYBRID EXCITON LANDSCAPE IN TMD BILAYERS

In here, we discuss how the exciton landscape in TMD bilayers is obtained within our theoretical framework, taking into account the effect of layer-hybridization. The starting-point is a two-dimensional system containing pure intra- and interlayer excitons. The intra- and interlayer exciton binding energies and wave functions in TMD bilayers are obtained from solving the bilayer Wannier equation [1]

$$\frac{\hbar^2 \mathbf{k}^2}{2m_{\text{red}}^{\xi L}} \varphi_{n,\mathbf{k}}^{\xi L} - \sum_{\mathbf{q}} V_{\mathbf{q}}^{c_{l_e} v_{l_h}} \varphi_{n,\mathbf{k}+\mathbf{q}}^{\xi L} = E_{n,\text{bind}}^{\xi L} \varphi_{n,\mathbf{k}}^{\xi L}, \quad (\text{S1})$$

where $\varphi_{n,\mathbf{k}}^{\xi L}$ is the excitonic wave function in state $n = 1s, 2s, \dots$, valley $\xi = (\xi_e, \xi_h)$, and layer $L = (l_e, l_h)$ and $E_{n,\text{bind}}^{\xi L}$ is the exciton binding energy. Here, the reduced exciton mass $m_{\text{red}}^{\xi L} = \frac{m^{\xi_e l_e} m^{\xi_h l_h}}{m^{\xi_h l_h} + m^{\xi_e l_e}}$, as well as the screened electron-hole Coulomb interaction $V_{\mathbf{q}}^{c_{l_e} v_{l_h}}$ enter. The valley-specific electron (hole) masses $m^{\xi_e l_e}$ ($m^{\xi_h l_h}$) are obtained from DFT calculations [2]. When evaluating the Coulomb matrix elements we explicitly include the finite thickness of the TMD layers as well as the dielectric environment via a generalized Keldysh screening [3]. In this work, we explicitly include hybridization of intra (X)- and interlayer (IX) excitons. In particular, the four possible intra- and interlayer exciton states (here expressed as $L \equiv IX_1, IX_2, X_1, X_2$ focusing on the energetically lowest $n = 1s$ transitions such that the exciton index can be omitted) are generally coupled by electron/hole tunneling. The resulting hybrid exciton states are obtained from diagonalizing the following exciton Hamiltonian [4, 5]

$$H_{x,0} = \sum_{\xi,L,\mathbf{Q}} E_{L,\mathbf{Q}}^{\xi} X_{L,\mathbf{Q}}^{\dagger \xi} X_{L,\mathbf{Q}}^{\xi} + \sum_{\xi,L,L',\mathbf{Q}} T_{LL'}^{\xi} X_{L,\mathbf{Q}}^{\dagger \xi} X_{L',\mathbf{Q}}^{\xi}, \quad (\text{S2})$$

containing the exciton centre-of-mass dispersion $E_{L,\mathbf{Q}}^{\xi} = \frac{\hbar^2 \mathbf{Q}^2}{2M^{\xi L}} + E_{\text{bind}}^{\xi L} + \Delta^{\xi L}$, $M^{\xi L} = m^{\xi_h l_h} + m^{\xi_e l_e}$ being the total exciton mass, $X^{(\dagger)}$ being excitonic and bosonic ladder operators and $\Delta^{\xi L}$ is the valley-specific band gap. The free Hamiltonian also contains a tunneling contribution which takes into account the tunneling of electrons and holes between different layers ($l_e \neq l'_e$ or $l_h \neq l'_h$) via the excitonic tunneling matrix element

$$T_{LL'}^{\xi} = F_{LL'}^{\xi} [T_{l_e l'_e}^{c_{l_e}} \delta_{l_h, l'_h} (1 - \delta_{l'_e, l_e}) - T_{l_h l'_h}^{v_{l_h}} \delta_{l_e, l'_e} (1 - \delta_{l'_h, l_h})]. \quad (\text{S3})$$

The excitonic tunneling matrix element crucially depends on electron and hole tunneling strengths, $T_{l_e l'_e}^{c_{l_e}}$ and $T_{l_h l'_h}^{v_{l_h}}$ respectively, as well as exciton wave function overlaps $F_{LL'}^{\xi} = \sum_{\mathbf{k}} \varphi_{\mathbf{k}}^{* \xi L} \varphi_{\mathbf{k}}^{\xi L'}$. The electron and hole tunneling strengths are obtained from *ab-initio* calculations and are reported in Ref. [4] for common TMD bilayers. For the considered case of 2H-stacked WSe₂ homobilayers we adopt the tunneling strengths $T^{cK} = 0$, $T^{vK} = 66.9$ meV and $T^{c\Lambda} = 236.6$ meV for the most relevant K/K' and Λ/Λ' valleys in this structure. Note that the electronic tunneling matrix elements are generally stacking- and momentum-dependent, however in this work we focus on naturally stacked (H_h^h) homobilayers, and evaluate the matrix elements at the high-symmetry points. The Hamiltonian in Eq. (S2) is now diagonalized via the basis transformation [5]

$$X_{L,\mathbf{Q}}^{\dagger \xi} = \sum_{\eta} C_L^{\xi \eta}(\mathbf{Q}) Y_{\eta,\mathbf{Q}}^{\dagger \xi}, \quad (\text{S4})$$

where $Y^{(\dagger)}$ is a new set of *hybrid* exciton operators and $C_L^{\xi \eta}(\mathbf{Q})$ is the *mixing coefficient* determining the relative intra/interlayer content of the hybrid exciton, enabling us to define a hybrid exciton state as $|hX_{\eta}\rangle = \sum_{i=1,2} (C_{X_i}^{\eta} |X_i\rangle +$

$C_{IX_i}^\eta |IX_i\rangle$) with $\sum_{i=1,2} (|C_{X_i}^\eta|^2 + |C_{IX_i}^\eta|^2) = 1$ for a fixed hybrid exciton state η . The mixing coefficients are obtained from solving the following hybrid eigenvalue problem[6]

$$E_{L,Q}^\xi C_L^{\xi\eta}(\mathbf{Q}) + \sum_{L'} T_{LL'}^\xi C_{L'}^{\xi\eta}(\mathbf{Q}) = E_{\eta,\mathbf{Q}}^{(hX)\xi} C_L^{\xi\eta}(\mathbf{Q}) , \quad (\text{S5})$$

introducing the hybrid exciton eigenenergy $E_{\eta,\mathbf{Q}}^{(hX)\xi}$. We can now express the exciton Hamiltonian above in the hybrid basis such that $H_{x,0} \rightarrow \tilde{H}_{x,0}$ with

$$\tilde{H}_{x,0} = \sum_{\xi,\eta,\mathbf{Q}} E_{\eta,\mathbf{Q}}^{(hX)\xi} Y_{\eta,\mathbf{Q}}^{\dagger\xi} Y_{\eta,\mathbf{Q}}^\xi . \quad (\text{S6})$$

By solving the eigenvalue problem in Eq. (S5) we get microscopic access to the full hybrid exciton landscape in TMD bilayers. Furthermore, we investigate the impact of an electric field on the hybrid exciton landscape. This is done by exploiting the electrostatic Stark shift of interlayer resonances, i.e. by taking $E_{L=IX,\mathbf{Q}}^\xi \rightarrow E_{L=IX,\mathbf{Q}}^\xi + \Delta E$, with $\Delta E = \pm d e_0 E_z$, where $d \approx 0.65$ nm is the dipole length (here assumed to be the same as the TMD layer thickness [7]), e_0 is the electric charge and E_z is the out-of-plane electric field [8]. In this way, hybrid exciton eigenenergies and mixing coefficients become tunable with respect to electric fields. In Table S1, we report the exciton hybrid energies and intralayer and interlayer mixing coefficients for hybrid excitons composed by electrons in the $\xi_e = \text{K}, \text{K}', \Lambda, \Lambda'$ valleys and holes in the $\xi_h = \text{K}, \text{K}'$ valleys in 2H-stacked hBN-encapsulated WSe₂ homobilayers. The energies are given relative to the intralayer A exciton energy and the electric fields $E_z = 0, \pm 0.3$ V/nm are considered.

Exciton	Energy $E - E_{X_A}$ (meV)			Intralayer component $ C_X ^2$			Interlayer component $ C_{IX} ^2$		
	$E_z = -0.3$	$E_z = 0$	$E_z = 0.3$	$E_z = -0.3$	$E_z = 0$	$E_z = 0.3$	$E_z = -0.3$	$E_z = 0$	$E_z = 0.3$
K Λ	-123	-159	-209	0.85	0.77	0.61	0.15	0.23	0.39
K' Λ'	-209	-159	-123	0.61	0.77	0.85	0.39	0.23	0.15
K Λ'	-12	-117	-258	0.58	0.36	0.2	0.42	0.64	0.8
K' Λ	-258	-117	-12	0.2	0.36	0.58	0.8	0.64	0.42
KK	-5	0	-179	0.96	1	0.01	0.04	0	0.99
K' K'	-179	0	-5	0.01	1	0.96	0.99	0	0.04
KK'	-58	-53	-137	0.96	1	0.01	0.04	0	0.99
K' K	-137	-53	-58	0.01	1	0.96	0.99	0	0.04

TABLE S1. Exciton landscape in hBN-encapsulated 2H-stacked WSe₂ homobilayers. We provide the valley-specific energies, intralayer components and interlayer components of hybrid excitons for three different values on the electric field, $E_z = 0, \pm 0.3$ V/nm. The energetically lowest transitions for each electric field are marked in bold and energies are given relative to the KK intralayer A exciton energy (E_{X_A}). For vanishing electric fields we find that the K Λ and K' Λ' states represent the energetically lowest states.

Note that the K Λ and K' Λ' exciton states are energetically degenerate at vanishing electric fields. This is a consequence of the H-type stacking, where the individual TMD layers are rotated 180 degrees with respect to each other such that the spin-orbit coupling in one of the layers is inverted. Moreover, these states can be expressed as $|K\Lambda\rangle = C_{X_1}^{K\Lambda} |X_1\rangle + C_{IX_1}^{K\Lambda} |IX_1\rangle$ and $|K'\Lambda'\rangle = C_{X_2}^{K'\Lambda'} |X_2\rangle + C_{IX_2}^{K'\Lambda'} |IX_2\rangle$ such that each of the states only mixes contributions from a single intralayer and a single interlayer exciton species. Hence, it follows that the K Λ and K' Λ' hX carry opposite out-of-plane dipole moments via their interlayer components, and therefore the energy of these states shifts in opposite directions under the application of an electric field (cf. Table S1).

II. HYBRID EXCITON-EXCITON INTERACTION HAMILTONIAN

Here, we provide a microscopic derivation of the hybrid exciton-exciton interaction Hamiltonian. The starting-point is the bilayer carrier-carrier Hamiltonian:

$$H_{c-c} = \frac{1}{2} \sum_{\lambda^{(')}, \xi^{(')}, l^{(')}} V_{\mathbf{q}}^{\lambda_l \lambda_{l'}} \lambda_{\xi, l, \mathbf{k} + \mathbf{q}}^{\dagger} \lambda_{\xi', l', \mathbf{k}' - \mathbf{q}}^{\dagger} \lambda_{\xi', l', \mathbf{k}'} \lambda_{\xi, l, \mathbf{k}}, \quad (\text{S7})$$

where $\lambda^{(')} = (c, v)$, ξ , and $l^{(')}$ are the band, valley, and layer indices, respectively. Here, the operators $\lambda^{(\dagger)}$ annihilate (create) carriers in band λ . Moreover, we note that $V_{\mathbf{q}}^{\lambda_l \lambda_{l'}}$ describes an intraband intralayer Coulomb interaction if $l = l'$ and an interlayer Coulomb interaction if $l \neq l'$. Furthermore, we consider the long-range part of the Coulomb interaction such that $V_{\mathbf{q}}^{\lambda_l \lambda_{l'}} \approx \frac{e_0^2}{2\epsilon_0 A |\mathbf{q}| \epsilon_{\text{intra}, \mathbf{q}}}$ and $V_{\mathbf{q}}^{\lambda_l \lambda_{l'}} \approx \frac{e_0^2}{2\epsilon_0 A |\mathbf{q}| \epsilon_{\text{inter}, \mathbf{q}}}$ ($l \neq \bar{l}$). The intra- and interlayer dielectric functions $\epsilon_{\text{intra}, \mathbf{q}}$ and $\epsilon_{\text{inter}, \mathbf{q}}$ can be found in the Supplementary Material of Ref. [9]. Interband Coulomb interactions, which give rise to electron-hole exchange [10] or Auger recombination [11], are not expected to contribute significantly to experimentally accessible density-dependent energy renormalizations (Supplementary Section IV) and are therefore neglected in this work.

Given the carrier-carrier Hamiltonian, we now proceed as follows: **i)** we find the equation of motion for the intervalley polarisation $\langle P_{\mathbf{k}_1 + \mathbf{Q}, \mathbf{k}_1}^{\dagger \xi_e l_e, \xi_h l_h} \rangle \equiv \langle c_{\xi_e, l_e, \mathbf{k}_1 + \mathbf{Q}}^{\dagger} v_{\xi_h, l_h, \mathbf{k}_1} \rangle$, **ii)** transform the equation of motion to the exciton basis [12], **iii)** make an ansatz for the exciton-exciton interaction Hamiltonian and compute the equation of motion for the polarisation in the exciton picture, **iv)** read off the exciton-exciton interaction matrix element such that the results from steps **ii)** and **iii)** coincide. Starting with the first step **i)**, we obtain the equation of motion for the polarisation directly from the Heisenberg equation of motion [1]. Including only the Coulomb contributions from Eq. (S7) we obtain

$$\begin{aligned} i\hbar \frac{d}{dt} \langle P_{\mathbf{k}_1 + \mathbf{Q}, \mathbf{k}_1}^{\dagger \xi_e l_e, \xi_h l_h} \rangle &= \frac{1}{2} \sum_{\mathbf{k}, \mathbf{q}, l, \xi} \left(V_{\mathbf{q}}^{v_l v_{l'}} \left(\langle c_{\xi_e, l_e, \mathbf{k}_1 + \mathbf{Q}}^{\dagger} v_{\xi_h, l_h, \mathbf{k}} v_{\xi_h, l_h, \mathbf{k}_1 - \mathbf{q}} v_{\xi, l, \mathbf{k} - \mathbf{q}}^{\dagger} \rangle - \langle c_{\xi_e, l_e, \mathbf{k}_1 + \mathbf{Q}}^{\dagger} v_{\xi_h, l_h, \mathbf{k}_1 - \mathbf{q}} v_{\xi, l, \mathbf{k}} v_{\xi, l, \mathbf{k} - \mathbf{q}}^{\dagger} \rangle \right) \right. \\ &+ V_{\mathbf{q}}^{c_l c_{l'}} \left(\langle c_{\xi, l, \mathbf{k} + \mathbf{q}}^{\dagger} v_{\xi_h, l_h, \mathbf{k}_1} c_{\xi_e, l_e, \mathbf{k}_1 + \mathbf{Q} - \mathbf{q}}^{\dagger} c_{\xi, l, \mathbf{k}} \rangle - \langle c_{\xi_e, l_e, \mathbf{k}_1 + \mathbf{Q} - \mathbf{q}}^{\dagger} v_{\xi_h, l_h, \mathbf{k}_1} c_{\xi, l, \mathbf{k} + \mathbf{q}}^{\dagger} c_{\xi, l, \mathbf{k}} \rangle \right) \\ &+ V_{\mathbf{q}}^{v_l c_{l'}} \left(\langle c_{\xi_e, l_e, \mathbf{k}_1 + \mathbf{Q} - \mathbf{q}}^{\dagger} v_{\xi_h, l_h, \mathbf{k}_1} v_{\xi, l, \mathbf{k}} v_{\xi, l, \mathbf{k} + \mathbf{q}}^{\dagger} \rangle - \langle c_{\xi_e, l_e, \mathbf{k}_1 + \mathbf{Q} - \mathbf{q}}^{\dagger} v_{\xi, l, \mathbf{k}} v_{\xi_h, l_h, \mathbf{k}_1} v_{\xi, l, \mathbf{k} + \mathbf{q}}^{\dagger} \rangle \right) \\ &\left. + V_{\mathbf{q}}^{v_l c_{l'}} \left(\langle c_{\xi_e, l_e, \mathbf{k}_1 + \mathbf{Q}}^{\dagger} v_{\xi_h, l_h, \mathbf{k}_1 - \mathbf{q}} c_{\xi, l, \mathbf{k} - \mathbf{q}}^{\dagger} c_{\xi, l, \mathbf{k}} \rangle - \langle c_{\xi, l, \mathbf{k} - \mathbf{q}}^{\dagger} v_{\xi_h, l_h, \mathbf{k}_1 - \mathbf{q}} c_{\xi_e, l_e, \mathbf{k}_1 + \mathbf{Q}}^{\dagger} c_{\xi, l, \mathbf{k}} \rangle \right) \right). \quad (\text{S8}) \end{aligned}$$

Next, we transform the entire equation above to the excitonic basis and make use of the pair operator expansions [12]

$$c_{\xi_e, l_e, \mathbf{k}}^{\dagger} c_{\xi_e', l_e', \mathbf{k}'} \approx \sum_{\xi_h'', l_h'', \mathbf{k}''} P_{\mathbf{k}, \mathbf{k}''}^{\dagger \xi_e l_e, \xi_h'' l_h''} P_{\mathbf{k}', \mathbf{k}''}^{\xi_e' l_e', \xi_h'' l_h''}, \quad v_{\xi_h, l_h, \mathbf{k}} v_{\xi_h', l_h', \mathbf{k}'} \approx \sum_{\xi_e'', l_e'', \mathbf{k}''} P_{\mathbf{k}'', \mathbf{k}}^{\dagger \xi_e'' l_e'', \xi_h l_h} P_{\mathbf{k}'', \mathbf{k}'}^{\xi_e'' l_e'', \xi_h' l_h'}, \quad (\text{S9})$$

where the pair operators can be further expressed in the exciton basis as $P_{\mathbf{k}, \mathbf{k}'}^{\xi_e l_e, \xi_h l_h} = \sum_n \varphi_{n, \beta \xi^L \mathbf{k} + \alpha \xi^L \mathbf{k}'}^{\xi} X_{n, L, \mathbf{k} - \mathbf{k}'}^{\xi}$, with $\varphi_{n, \mathbf{k}}^{\xi L}$ being the exciton wave function (cf. Supplementary Section I) and the compound indices $\xi = (\xi_e, \xi_h)$, $L = (l_e, l_h)$ (such that $l_e = l_h$ corresponds to the intralayer wave function and $l_e \neq l_h$ corresponds to the interlayer wave function). In the following, we will only consider the lowest-lying $n = 1s$ exciton states, so that the index n can be omitted. By doing this, the equation of motion Eq. (S8) separates into two parts, a direct part and an exchange part. The second, fourth, fifth and seventh term in Eq. (S8) gives rise to the direct terms reading

$$\begin{aligned} i\hbar \frac{d}{dt} \langle X_{L', \mathbf{Q}}^{\dagger \xi'} \rangle |_{\text{dir.}} &= \frac{1}{2} \sum_{\mathbf{q}, \mathbf{Q}_1, \xi, L} \left(V_{\mathbf{q}}^{c_{l_e} v_{l_h}} F(\alpha^{\xi' L'} \mathbf{q}) F(\beta^{\xi L} \mathbf{q}) + V_{\mathbf{q}}^{c_{l_e} v_{l_h}} F(-\alpha^{\xi' L'} \mathbf{q}) F(-\beta^{\xi L} \mathbf{q}) \right. \\ &\left. - V_{\mathbf{q}}^{c_{l_e} c_{l_e'}} F(\beta^{\xi' L'} \mathbf{q}) F(-\beta^{\xi L} \mathbf{q}) - V_{\mathbf{q}}^{v_{l_h} v_{l_h'}} F(-\alpha^{\xi' L'} \mathbf{q}) F(\alpha^{\xi L} \mathbf{q}) \right) \langle X_{L', \mathbf{Q} + \mathbf{q}}^{\dagger \xi'} X_{L, \mathbf{Q}_1 - \mathbf{q}}^{\dagger \xi} X_{L, \mathbf{Q}_1}^{\xi} \rangle, \quad (\text{S10}) \end{aligned}$$

where we introduced the compound indices $\xi^{(')} = (\xi_e^{(')}, \xi_h^{(')})$ and $L^{(')} = (l_e^{(')}, l_h^{(')})$. Here, we also defined the excitonic form factors $F(x^{\xi L} \mathbf{q}) \equiv \sum_{\mathbf{k}} \varphi_{\mathbf{k} + x^{\xi L} \mathbf{q}}^{\xi L} \varphi_{\mathbf{k}}^{\xi L}$. We may now construct the corresponding direct exciton-exciton interaction Hamiltonian with

$$H_{x-x} |_{\text{dir.}} = \frac{1}{2} \sum_{\substack{\mathbf{Q}_1, \mathbf{Q}_2, \mathbf{q} \\ \xi, \xi', L, L'}} D_{L, L', \mathbf{q}}^{\xi \xi'} X_{L', \mathbf{Q}_1 + \mathbf{q}}^{\dagger \xi'} X_{L, \mathbf{Q}_2 - \mathbf{q}}^{\dagger \xi} X_{L, \mathbf{Q}_2}^{\xi} X_{L', \mathbf{Q}_1}^{\xi'}, \quad (\text{S11})$$

with the direct part of the exciton-exciton interaction reading

$$D_{L,L',\mathbf{q}}^{\xi\xi'} = \frac{1}{2} \left(V_{\mathbf{q}}^{c_{1e}c_{1e}'} F(\beta^{\xi L'} \mathbf{q}) F(-\beta^{\xi L} \mathbf{q}) + V_{\mathbf{q}}^{v_{1h}v_{1h}'} F(-\alpha^{\xi' L'} \mathbf{q}) F(\alpha^{\xi L} \mathbf{q}) \right. \\ \left. - V_{\mathbf{q}}^{c_{1e}v_{1h}'} F(\alpha^{\xi' L'} \mathbf{q}) F(\beta^{\xi L} \mathbf{q}) - V_{\mathbf{q}}^{v_{1h}c_{1e}'} F(-\alpha^{\xi' L'} \mathbf{q}) F(-\beta^{\xi L} \mathbf{q}) \right), \quad (\text{S12})$$

such that a commutation of the excitonic Hamiltonian (S11) with the polarisation gives rise to Eq. (S10). We note that, in the long wavelength limit

$$D_{X_i, X_i, \mathbf{0}}^{\xi\xi'} = D_{X_i, X_j, \mathbf{0}}^{\xi\xi'} = 0, \quad D_{IX_i, IX_i, \mathbf{0}}^{\xi\xi'} = -D_{IX_i, IX_j, \mathbf{0}}^{\xi\xi'} = \frac{e_0^2}{4A\epsilon_0} \left(\frac{d_{1,\text{TMD}}}{\epsilon_{1,\text{TMD}}^\perp} + \frac{d_{2,\text{TMD}}}{\epsilon_{2,\text{TMD}}^\perp} \right), \quad i \neq j \quad (\text{S13})$$

i.e. we find a vanishing direct interaction between intralayer excitons ($L, L' = X_i, i = 1, 2$) and recover the widely used plate capacitor formula when considering interactions between interlayer excitons ($L, L' = IX_i, i = 1, 2$) as has been previously confirmed in literature [11, 13, 14]. Here, the material-specific constants $d_{i,\text{TMD}}$ and $\epsilon_{i,\text{TMD}}^\perp$ denote individual TMD monolayer thicknesses and out-of-plane components of the TMD dielectric tensors, respectively. In the main manuscript we set $d_{1,\text{TMD}} = d_{2,\text{TMD}} \equiv d_{\text{TMD}}$ and $\epsilon_{1,\text{TMD}}^\perp = \epsilon_{2,\text{TMD}}^\perp \equiv \epsilon_{\text{TMD}}^\perp$ as we are considering a homobilayer. Note that interactions between different interlayer exciton species IX_i and $IX_j, i \neq j$ are attractive due to the opposite dipole orientations of these excitons. Now, we consider the remaining terms (i.e. the first, third, fifth and eighth terms) in Eq. (S8) and find that these give rise to the following exchange terms

$$i\hbar \frac{d}{dt} \langle X_{L',\mathbf{Q}}^{\dagger\xi'} |_{\text{exch.}} = \frac{1}{2} \sum_{\substack{\mathbf{q}, \mathbf{Q}_1, \mathbf{k}, \mathbf{k}' \\ \xi, \xi, \bar{\xi} \\ L, \bar{L}, \bar{L}}} \left((V_{\mathbf{k}-\mathbf{k}'}^{c_{1e}c_{1e}'} \varphi_{\mathbf{k}-\alpha^{\xi' L'} \mathbf{Q}-\mathbf{q}}^{\xi' L'} - V_{\mathbf{k}-\mathbf{k}'}^{c_{1e}v_{1h}'} \varphi_{\mathbf{k}'-\alpha^{\xi' L'} \mathbf{Q}-\mathbf{q}}^{\xi' L'}) \times \right. \\ \delta_{l_h, l'_h}^{\xi_h, \xi'_h} \delta_{l_e, l'_e}^{\xi_e, \xi'_e} \delta_{l_e, l'_e}^{\bar{\xi}_e, \bar{\xi}'_e} \delta_{l_h, l'_h}^{\bar{\xi}_h, \bar{\xi}'_h} \varphi_{\mathbf{k}-\alpha^{\xi L} (\mathbf{Q}+\mathbf{q})}^{*\xi L} \varphi_{\mathbf{k}'-\beta^{\bar{\xi} \bar{L}} \mathbf{q}-\alpha^{\bar{\xi} \bar{L}} \mathbf{Q}_1}^{*\bar{\xi} \bar{L}} \varphi_{\mathbf{k}'-\alpha^{\bar{\xi} \bar{L}} \mathbf{Q}_1}^{\bar{\xi} \bar{L}} \\ + (V_{\mathbf{k}-\mathbf{k}'}^{v_{1h}v_{1h}'} \varphi_{\mathbf{k}+\beta^{\xi' L'} \mathbf{Q}+\mathbf{q}}^{\xi' L'} - V_{\mathbf{k}-\mathbf{k}'}^{c_{1e}v_{1h}'} \varphi_{\mathbf{k}'+\beta^{\xi' L'} \mathbf{Q}+\mathbf{q}}^{\xi' L'}) \times \\ \left. \delta_{l_e, l'_e}^{\xi_e, \xi'_e} \delta_{l_h, l'_h}^{\bar{\xi}_h, \xi'_h} \delta_{l_e, l'_e}^{\bar{\xi}_e, \bar{\xi}'_e} \delta_{l_h, l'_h}^{\bar{\xi}_h, \xi_h} \varphi_{\mathbf{k}+\beta^{\xi L} (\mathbf{Q}+\mathbf{q})}^{*\xi L} \varphi_{\mathbf{k}'+\alpha^{\bar{\xi} \bar{L}} \mathbf{q}+\beta^{\bar{\xi} \bar{L}} \mathbf{Q}_1}^{*\bar{\xi} \bar{L}} \varphi_{\mathbf{k}'+\beta^{\bar{\xi} \bar{L}} \mathbf{Q}_1}^{\bar{\xi} \bar{L}} \right) \times \\ \langle X_{L, \mathbf{Q}+\mathbf{q}}^{\dagger\xi} X_{\bar{L}, \mathbf{Q}_1-\mathbf{q}}^{\dagger\bar{\xi}} X_{\bar{L}, \mathbf{Q}_1}^{\bar{\xi}} \rangle \quad (\text{S14})$$

from which we may construct an exchange matrix element such that

$$\frac{d}{dt} \langle X_{L',\mathbf{Q}}^{\dagger\xi'} |_{\text{exch.}} = \frac{i}{\hbar} \sum_{\substack{\mathbf{q}, \mathbf{Q}_1 \\ \xi, \xi, \bar{\xi} \\ L, \bar{L}, \bar{L}}} E_{L, \bar{L}, L', \mathbf{Q}, \mathbf{Q}_1, \mathbf{q}}^{\xi \bar{\xi} \xi \xi'} \langle X_{L, \mathbf{Q}+\mathbf{q}}^{\dagger\xi} X_{\bar{L}, \mathbf{Q}_1-\mathbf{q}}^{\dagger\bar{\xi}} X_{\bar{L}, \mathbf{Q}_1}^{\bar{\xi}} \rangle, \quad (\text{S15})$$

where the exchange part of the exciton-exciton interaction reads

$$E_{L_1, L_2, L_3, L_4, \mathbf{Q}_1, \mathbf{Q}_2, \mathbf{q}}^{\xi_1 \xi_2 \xi_3 \xi_4} = \frac{1}{2} \sum_{\mathbf{k}, \mathbf{k}'} \left((V_{\mathbf{k}-\mathbf{k}'}^{c_{1e}c_{1e}'} \varphi_{\mathbf{k}'-\alpha^{\xi_4 L_4} \mathbf{Q}_1-\mathbf{q}}^{\xi_4 L_4} - V_{\mathbf{k}-\mathbf{k}'}^{c_{1e}c_{1e}'} \varphi_{\mathbf{k}-\alpha^{\xi_4 L_4} \mathbf{Q}_1-\mathbf{q}}^{\xi_4 L_4}) \times \right. \\ \delta_{l_{1,h}, l_{1,h}}^{\xi_{1,h}, \xi_{4,h}} \delta_{l_{2,e}, l_{4,e}}^{\xi_{2,e}, \xi_{4,e}} \delta_{l_{3,e}, l_{1,e}}^{\xi_{3,e}, \xi_{1,e}} \delta_{l_{3,h}, l_{2,h}}^{\xi_{3,h}, \xi_{2,h}} \varphi_{\mathbf{k}-\alpha^{\xi_1 L_1} (\mathbf{Q}_1+\mathbf{q})}^{*\xi_1 L_1} \varphi_{\mathbf{k}'-\beta^{\xi_2 L_2} \mathbf{q}-\alpha^{\xi_2 L_2} \mathbf{Q}_2}^{*\xi_2 L_2} \varphi_{\mathbf{k}'-\alpha^{\xi_3 L_3} \mathbf{Q}_2}^{\xi_3 L_3} \\ + (V_{\mathbf{k}-\mathbf{k}'}^{c_{1e}c_{1e}'} \varphi_{\mathbf{k}'+\beta^{\xi_4 L_4} \mathbf{Q}_1+\mathbf{q}}^{\xi_4 L_4} - V_{\mathbf{k}-\mathbf{k}'}^{v_{1h}v_{1h}'} \varphi_{\mathbf{k}+\beta^{\xi_4 L_4} \mathbf{Q}_1+\mathbf{q}}^{\xi_4 L_4}) \times \\ \left. \delta_{l_{1,e}, l_{4,e}}^{\xi_{1,e}, \xi_{4,e}} \delta_{l_{2,h}, l_{4,h}}^{\xi_{2,h}, \xi_{4,h}} \delta_{l_{3,e}, l_{2,e}}^{\xi_{3,e}, \xi_{2,e}} \delta_{l_{3,h}, l_{1,h}}^{\xi_{3,h}, \xi_{1,h}} \varphi_{\mathbf{k}+\beta^{\xi_1 L_1} (\mathbf{Q}_1+\mathbf{q})}^{*\xi_1 L_1} \varphi_{\mathbf{k}'+\alpha^{\xi_2 L_2} \mathbf{q}+\beta^{\xi_2 L_2} \mathbf{Q}_2}^{*\xi_2 L_2} \varphi_{\mathbf{k}'+\beta^{\xi_3 L_3} \mathbf{Q}_2}^{\xi_3 L_3} \right). \quad (\text{S16})$$

Here, we note that the first term corresponds to hole-hole exchange within the excitons and the second term corresponds to electron-electron exchange. In particular, the Kronecker deltas imply that fermionic exchange of individual charge constituents is only allowed if charges of the same species reside in the same layer and valley. Moreover, the exchange interaction is generally dependent on both centre-of-mass momenta $\mathbf{Q}_1, \mathbf{Q}_2$ as well as the relative momentum \mathbf{q} . In the long wavelength limit ($q, Q_1, Q_2 \ll a_B^{-1}$, a_B being the exciton Bohr radius) the exchange interaction is non-vanishing for both intra- and interlayer exciton species, and it is the dominating contribution to the exciton-exciton

interaction for intralayer excitons [13, 15, 16]. However, we remark that the resulting density-dependent energy renormalizations due to intralayer exchange interactions are negligible (see Supplementary Section IV). Exchange interactions are therefore not considered in the main manuscript, but included here only for the sake of completeness. Hence, we obtain the exchange part of the exciton-exciton Hamiltonian

$$H_{x-x}|_{\text{exch.}} = \frac{1}{2} \sum_{\substack{\mathbf{Q}_1, \mathbf{Q}_2, \mathbf{q} \\ \xi_1 \dots \xi_4 \\ L_1 \dots L_4}} E_{L_1, L_2, L_3, L_4, \mathbf{Q}_1, \mathbf{Q}_2, \mathbf{q}}^{\xi_1 \xi_2 \xi_3 \xi_4} X_{L_1, \mathbf{Q}_1 + \mathbf{q}}^{\dagger \xi_1} X_{L_2, \mathbf{Q}_2 - \mathbf{q}}^{\dagger \xi_2} X_{L_3, \mathbf{Q}_2}^{\xi_3} X_{L_4, \mathbf{Q}_1}^{\xi_4}. \quad (\text{S17})$$

We now have access to the multilayer exciton-exciton interaction involving both intra- and interlayer excitons. However, generally, excitons are hybridized between the layers due to electron/hole tunneling. To include the effect of hybridization, we transform the excitonic operators to the hybrid basis, cf. Eq. (S4). The exciton-exciton Hamiltonian then transforms into a hybrid Hamiltonian

$$\tilde{H}_{x-x} = \frac{1}{2} \sum_{\substack{\eta_1 \dots \eta_4 \\ \xi_1 \dots \xi_4 \\ \mathbf{Q}_1, \mathbf{Q}_2, \mathbf{q}}} \tilde{W}_{\eta_1, \eta_2, \eta_3, \eta_4, \mathbf{Q}_1, \mathbf{Q}_2, \mathbf{q}}^{\xi_1 \xi_2 \xi_3 \xi_4} Y_{\eta_1, \mathbf{Q}_1 + \mathbf{q}}^{\dagger \xi_1} Y_{\eta_2, \mathbf{Q}_2 - \mathbf{q}}^{\dagger \xi_2} Y_{\eta_3, \mathbf{Q}_2}^{\xi_3} Y_{\eta_4, \mathbf{Q}_1}^{\xi_4}, \quad (\text{S18})$$

where the hybrid exciton-exciton interaction contains of a direct part and an exchange part according to

$$\tilde{D}_{\eta_1, \eta_2, \eta_3, \eta_4, \mathbf{Q}_1, \mathbf{Q}_2, \mathbf{q}}^{\xi_1 \xi_2} = \sum_{L_1, L_2} D_{L_1, L_2, \mathbf{q}}^{\xi_1 \xi_2} C_{L_1, \mathbf{Q}_1 + \mathbf{q}}^{* \xi_1 \eta_1} C_{L_1, \mathbf{Q}_1}^{\xi_1 \eta_4} C_{L_2, \mathbf{Q}_2 - \mathbf{q}}^{* \xi_2 \eta_2} C_{L_2, \mathbf{Q}_2}^{\xi_2 \eta_3}, \quad (\text{S19})$$

and

$$\tilde{E}_{\eta_1, \eta_2, \eta_3, \eta_4, \mathbf{Q}_1, \mathbf{Q}_2, \mathbf{q}}^{\xi_1 \xi_2 \xi_3 \xi_4} = \sum_{L_1, L_2, L_3, L_4} E_{L_1, L_2, L_3, L_4, \mathbf{Q}_1, \mathbf{Q}_2, \mathbf{q}}^{\xi_1 \xi_2 \xi_3 \xi_4} C_{L_1, \mathbf{Q}_1 + \mathbf{q}}^{* \xi_1 \eta_1} C_{L_4, \mathbf{Q}_1}^{\xi_4 \eta_4} C_{L_2, \mathbf{Q}_2 - \mathbf{q}}^{* \xi_2 \eta_2} C_{L_3, \mathbf{Q}_2}^{\xi_3 \eta_3}, \quad (\text{S20})$$

with the unhybridised direct (D) and exchange (E) matrix elements defined in Eq. (S12) and (S16), respectively. Having derived the most general form of the hybrid exciton-exciton interaction, we now remark on the considered case of untwisted homobilayers. In this case, it holds that the mixing coefficients are approximately constant in momentum, such that $C_L^{\xi \eta} \approx C_L^{\xi \eta}$ [4]. Consequently, the direct hybrid exciton-exciton interaction depends only on the relative momentum \mathbf{q} . In the main manuscript, we only consider the lowest-lying hybrid exciton states for each valley configuration and therefore the indices η_i , $i = 1 \dots 4$ are omitted therein. Moreover, note that the intra- and interlayer mixing coefficients enter the hybrid exciton-exciton interaction strengths. This provides an intriguing way of tuning the interaction strength with externally applied electric fields.

III. DIPOLE-DIPOLE INTERACTION

In here, we show that the real-space representation of the direct interlayer exciton-exciton interaction (Eq. (S12), with $L = L' = IX$ and $\xi = \xi'$) can be interpreted as a classical dipole-dipole interaction at large distances. By considering the two TMD layers forming the homobilayer as two infinitely thin slabs separated by the distance d and approximating the dielectric environment as homogenous, with a single effective dielectric constant ϵ_{BL} , we find an analytic expression for the direct exciton-exciton interaction. Within these approximations, the intra (X)- and interlayer (IX) Coulomb interactions read [3]

$$V_{\mathbf{q}}^X = \frac{e_0^2}{2\epsilon_0 A |\mathbf{q}| \epsilon_{\text{BL}}}, V_{\mathbf{q}}^{IX} = \frac{e_0^2}{2\epsilon_0 A |\mathbf{q}| \epsilon_{\text{BL}} (1 + \tanh(|\mathbf{q}|d))}. \quad (\text{S21})$$

Now, substituting these simplified expressions into the direct exciton-exciton interaction and setting the excitonic form factors $F \approx 1$, we find that the direct interlayer exciton-exciton interaction reduces to

$$D_{IX, IX, \mathbf{q}} \approx \frac{e_0^2}{2\epsilon_0 A |\mathbf{q}| \epsilon_{\text{BL}}} \left(1 - \frac{1}{1 + \tanh(|\mathbf{q}|d)}\right). \quad (\text{S22})$$

The real-space representation of the interaction is obtained by taking the Fourier-transform:

$$D_{IX, IX}(\mathbf{r}) = \frac{e_0^2}{4\pi\epsilon_0 \epsilon_{\text{BL}}} \left(\frac{1}{|\mathbf{r}|} - \frac{1}{d(\sqrt{4 + |\mathbf{r}|^2/d^2})}\right). \quad (\text{S23})$$

Finally, we are interested in the asymptotic behavior of the interaction and therefore let $r \gg d$. In this limit, we find

$$D_{IX,IX}(\mathbf{r}) = \frac{d^2 e_0^2}{2\pi \epsilon_0 \epsilon_{\text{BL}}} \frac{1}{|\mathbf{r}|^3} + \mathcal{O}(|\mathbf{r}|^{-5}), \quad (\text{S24})$$

which is precisely a classical dipole-dipole interaction. Now, as the interlayer components of the mixing coefficients are approximately constant in momentum (cf. Supplementary Section I) for untwisted TMD homobilayers, we note that also the corresponding real-space hybrid exciton-exciton interaction obeys the asymptotic $1/r^3$ behavior for large r . In Fig. S1, we show the direct hybrid exciton-exciton interaction strength between KA excitons in hBN-encapsulated WSe_2 homobilayers as a function of distance, r , including the dominant interlayer contributions to the interaction (solid yellow curve). Unlike in the main manuscript, we here plot the logarithm of the interaction strength over large distances. Importantly, we find that the interaction scales as $1/r^3$ (dashed black curve) at distances $r \gtrsim 15$ nm. This confirms the dipole-dipole-like character of the hybrid exciton-exciton interaction at large distances.

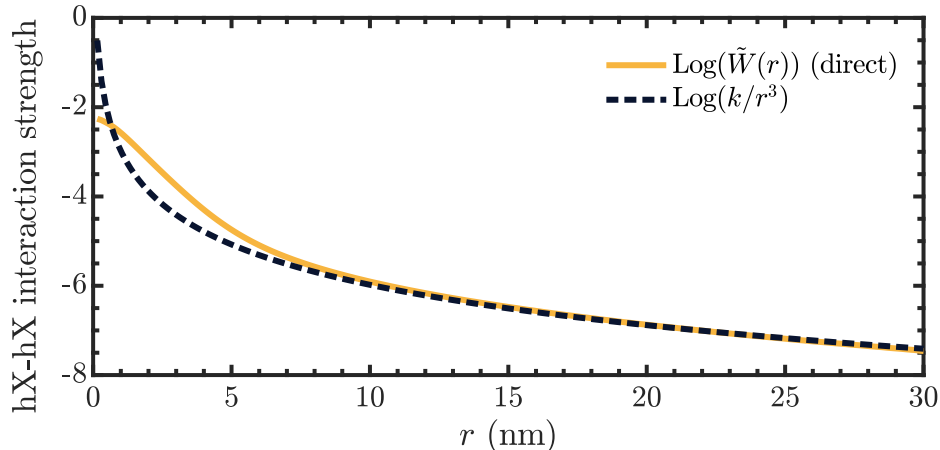


FIG. S1. Real-space representation of the hybrid exciton-exciton interaction for KA excitons. Note that we here have taken the logarithm of the interaction strength.

IV. DENSITY-DEPENDENT ENERGY RENORMALIZATIONS FOR HYBRID EXCITONS

Having access to the microscopic hybrid exciton-exciton Hamiltonian (Eq. (S18) and Supplementary Section II) implies that we are now also able to investigate density-dependent energy renormalizations of hybrid excitons. These energy renormalizations can be derived from the corresponding Heisenberg equation of motion for the (hybrid) polarisation $\langle Y_{\zeta, \mathbf{Q}}^\dagger \rangle$ reading

$$\frac{d}{dt} \langle Y_{\zeta, \mathbf{Q}}^\dagger \rangle = \frac{i}{\hbar} \sum_{\mathbf{Q}_1, \mathbf{q}, \zeta_1, \zeta_2, \zeta_3} \tilde{W}_{\mathbf{Q}, \mathbf{Q}_1, \mathbf{q}}^{\zeta_1 \zeta_2 \zeta_3 \zeta} \langle Y_{\zeta_1, \mathbf{Q}+\mathbf{q}}^\dagger Y_{\zeta_2, \mathbf{Q}_1-\mathbf{q}}^\dagger Y_{\zeta_3, \mathbf{Q}_1} \rangle, \quad (\text{S25})$$

where we introduced the compound index $\zeta = (\xi, \eta)$ including the valley index ξ and the hybrid exciton index η . Now, we consider the equation above on a Hartree-Fock level, i.e. we expand the appearing bosonic three-operator expectation value into single-particle expectation values and neglect two-particle correlations. We also make use of the random phase approximation (RPA) [1] such that the equation above becomes

$$\frac{d}{dt} \langle Y_{\zeta, \mathbf{Q}}^\dagger \rangle \approx \frac{i}{\hbar} \sum_{\mathbf{q}, \zeta_1} (\tilde{W}_{\mathbf{Q}, \mathbf{q}, 0}^{\zeta \zeta_1 \zeta_1 \zeta} + \tilde{W}_{\mathbf{Q}, \mathbf{q}, \mathbf{q}-\mathbf{Q}}^{\zeta_1 \zeta \zeta_1 \zeta}) N_{\mathbf{q}}^{\zeta_1} \langle Y_{\zeta, \mathbf{Q}}^\dagger \rangle, \quad (\text{S26})$$

where we defined the hybrid exciton occupation $N_{\mathbf{Q}}^{\zeta} \equiv \langle Y_{\zeta, \mathbf{Q}}^\dagger Y_{\zeta, \mathbf{Q}} \rangle$. Here we also approximated $\langle Y_{\zeta, \mathbf{Q}}^\dagger Y_{\zeta', \mathbf{Q}'} \rangle \approx \delta_{\mathbf{Q}, \mathbf{Q}'}^{\zeta, \zeta'} N_{\mathbf{Q}}^{\zeta}$ making use of the RPA. Note that the energy renormalization consists of two terms, the first term being a direct term and the second being an exchange term, with the latter reflecting exciton exchange [13]. In contrast to the exchange interaction \tilde{E} which includes exchange of individual carriers, the exciton exchange takes into account the exchange of

individual excitons. Furthermore, we consider low temperatures in this work such that the exciton distribution $N_{\mathbf{q}}$ is strongly peaked around $\mathbf{q} = 0$ and assume the centre-of-mass momentum $|\mathbf{Q}| \ll a_B^{-1}$, where a_B is the exciton Bohr radius. This reduces the equation above to $\frac{d}{dt} \langle Y_{\zeta, \mathbf{Q}}^\dagger \rangle \approx \frac{i}{\hbar} \delta E^\zeta \langle Y_{\zeta, \mathbf{Q}}^\dagger \rangle$ introducing the energy renormalization

$$\delta E^\zeta = A \sum_{\zeta_1} (\tilde{W}_{0,0,0}^{\zeta_1 \zeta \zeta_1 \zeta} + \tilde{W}_{0,0,0}^{\zeta \zeta_1 \zeta_1 \zeta}) n_x^{\zeta_1}, \quad (\text{S27})$$

where $n_x^{\zeta_1} \equiv \frac{1}{A} \sum_{\mathbf{Q}} N_{\mathbf{Q}}^{\zeta_1}$ with A being the crystal area (cancelling out with the area A in the electronic Coulomb matrix elements). Finally, we restrict ourselves to the energetically lowest hybrid exciton states in this work such that the compound index ζ reduces to the valley index ξ . Generally, the energy renormalization of a hybrid exciton ξ is obtained by taking into account the interactions between all the different exciton species. By assuming that $n_x^\xi \propto n_x$, i.e. assuming a thermalized Boltzmann distribution for the hybrid excitons, where $n_x = \sum_{\xi} n_x^\xi$ is the total exciton density, the energy renormalization of a single exciton species can be quantified by a valley-specific effective dipole length d^ξ obtained from

$$\delta E^\xi = A \sum_{\xi_1} (\tilde{W}_{0,0,0}^{\xi_1 \xi \xi_1 \xi} + \tilde{W}_{0,0,0}^{\xi \xi_1 \xi_1 \xi}) n_x^{\xi_1} \equiv \frac{d^\xi e_0^2}{\epsilon_0 \epsilon_{\text{TMD}}^\perp} n_x. \quad (\text{S28})$$

In the evaluation of valley-specific dipole lengths we here only include the direct (dipole-dipole) contributions to the hybrid exciton-exciton interaction, cf. Eq. (S18). This is done as interlayer exchange interactions are seen to provide a small quantitative correction to the dipole-dipole interaction [9]. Moreover, although intralayer exchange interactions taking into account individual exchange of carriers are dominant in TMD monolayers [11, 14], they have negligible impact on the energy renormalizations, as their contributions are largely cancelled out against contributions due to higher-order correlations such as biexcitons [10]. This goes beyond the scope of the Hartree-Fock theory presented in this work.

In Fig. S2 we illustrate the valley-specific effective dipole length as obtained from Eq. (S28) for the case of naturally stacked hBN-encapsulated WSe₂ homobilayers as a function of electric field, E_z at low temperatures, $T = 10$ K. Intriguingly, we find a drastic increase in the dipole length at around $E_z \pm 0.15$ V/nm. This reflects the transition from a mostly intralayer $\text{K}\Lambda$ ($\text{K}'\Lambda'$) state to a mostly interlayer $\text{K}\Lambda'$ ($\text{K}'\Lambda$) state under the application of a positive (negative) electric field. At vanishing electric fields, $\text{K}\Lambda$ and $\text{K}'\Lambda'$ excitons coexist. These excitons independently interact via weak repulsive dipole-dipole interactions and mutually interact with each other via attractive dipolar interactions as they exhibit opposite dipole orientations, giving rise to negligible effective dipole lengths. At the largest considered electric fields, $E_z = 0.3$ V/nm, only $\text{K}\Lambda'$ excitons are relevant and the impact of other excitons is negligible due to the large energy separations between exciton states (cf. Table S1). These excitons are mostly interlayer-like in nature ($|C_{IX}|^2 = 0.8$, cf. Table S1) and interact strongly via dipole-dipole repulsion. Note that the large effective dipole moment of $\text{K}\Lambda'$ excitons directly translates into large energy renormalizations (Eq. (S28)) and give rise to sizable blue-shifts of phonon sidebands with exciton density, as schematically illustrated by the inset in Fig. S2.

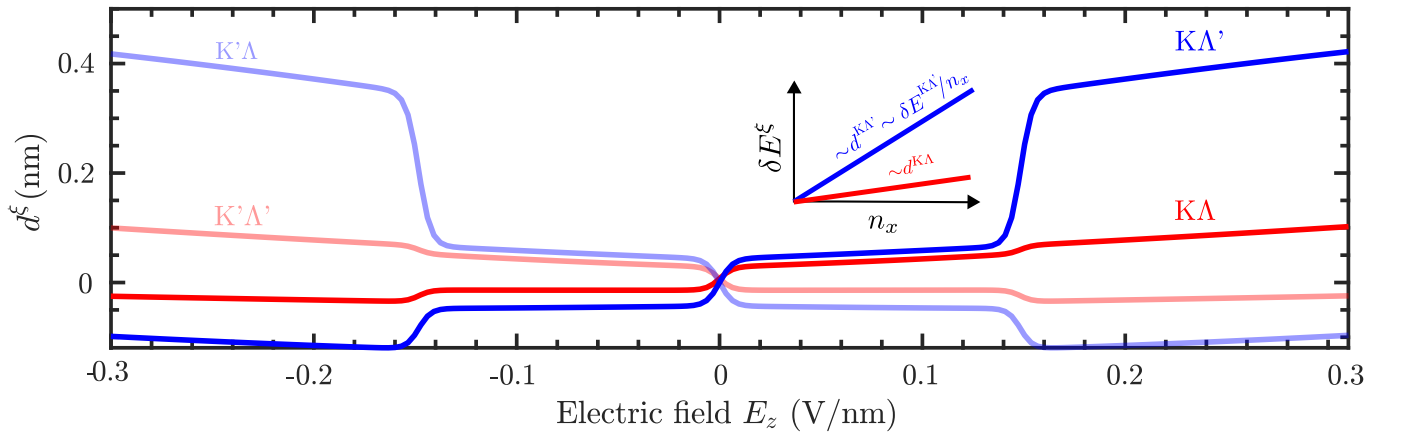


FIG. S2. Valley-specific effective dipole length in naturally stacked hBN-encapsulated WSe₂ homobilayers. The valley-specific dipole length d^ξ determines the corresponding energy renormalization $\delta E^\xi \sim d^\xi n_x$ for an individual exciton species ξ (cf. inset).

-
- [1] M. Kira and S. W. Koch, Many-body correlations and excitonic effects in semiconductor spectroscopy, *Progress in quantum electronics* **30**, 155 (2006).
 - [2] A. Kormányos, G. Burkard, M. Gmitra, J. Fabian, V. Zólyomi, N. D. Drummond, and V. Fal'ko, k·p theory for two-dimensional transition metal dichalcogenide semiconductors, *2D Materials* **2**, 022001 (2015).
 - [3] S. Ovesen, S. Brem, C. Linderålv, M. Kuisma, T. Korn, P. Erhart, M. Selig, and E. Malic, Interlayer exciton dynamics in van der Waals heterostructures, *Communications Physics* **2**, 1 (2019).
 - [4] J. Hagel, S. Brem, C. Linderålv, P. Erhart, and E. Malic, Exciton landscape in van der Waals heterostructures, *Physical Review Research* **3**, 043217 (2021).
 - [5] S. Brem, K.-Q. Lin, R. Gillen, J. M. Bauer, J. Maultzsch, J. M. Lupton, and E. Malic, Hybridized intervalley moiré excitons and flat bands in twisted WSe₂ bilayers, *Nanoscale* **12**, 11088 (2020).
 - [6] S. Brem, C. Linderålv, P. Erhart, and E. Malic, Tunable phases of moiré excitons in van der Waals heterostructures, *Nano Letters* **20**, 8534 (2020).
 - [7] A. Laturia, M. L. Van de Put, and W. G. Vandenberghe, Dielectric properties of hexagonal boron nitride and transition metal dichalcogenides: from monolayer to bulk, *npj 2D Materials and Applications* **2**, 1 (2018).
 - [8] J. Hagel, S. Brem, and E. Malic, Electrical tuning of moiré excitons in mose2 bilayers, *2D Materials* **10**, 014013 (2022).
 - [9] D. Erkensten, S. Brem, R. Perea-Causín, and E. Malic, Microscopic origin of anomalous interlayer exciton transport in van der Waals heterostructures, *Physical Review Materials* **6**, 094006 (2022).
 - [10] F. Katsch, M. Selig, and A. Knorr, Theory of coherent pump-probe spectroscopy in monolayer transition metal dichalcogenides, *2D Materials* **7**, 015021 (2019).
 - [11] D. Erkensten, S. Brem, and E. Malic, Exciton-exciton interaction in transition metal dichalcogenide monolayers and van der Waals heterostructures, *Physical Review B* **103**, 045426 (2021).
 - [12] F. Katsch, M. Selig, A. Carmele, and A. Knorr, Theory of exciton-exciton interactions in monolayer transition metal dichalcogenides, *physica status solidi (b)* **255**, 1800185 (2018).
 - [13] C. Ciuti, V. Savona, C. Piermarocchi, A. Quattropani, and P. Schwendimann, Role of the exchange of carriers in elastic exciton-exciton scattering in quantum wells, *Physical Review B* **58**, 7926 (1998).
 - [14] V. Shahnazaryan, I. Iorsh, I. A. Shelykh, and O. Kyriienko, Exciton-exciton interaction in transition-metal dichalcogenide monolayers, *Physical Review B* **96**, 115409 (2017).
 - [15] C. Schindler and R. Zimmermann, Analysis of the exciton-exciton interaction in semiconductor quantum wells, *Physical Review B* **78**, 045313 (2008).
 - [16] F. Tassone and Y. Yamamoto, Exciton-exciton scattering dynamics in a semiconductor microcavity and stimulated scattering into polaritons, *Physical Review B* **59**, 10830 (1999).